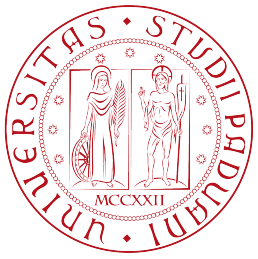

UNIVERSITÀ DEGLI STUDI DI PADOVA

Dipartimento di Fisica e Astronomia "Galileo Galilei"

Master Degree in Physics

Final Dissertation

Creation, validation and application of a collisional radiative model for positive Argon ions

Thesis supervisor
Dr. Gianluigi Serianni
Thesis co-supervisors
Prof. Dr. Ing. Ursel Fantz
Dr. Dirk Wünderlich

Candidate
Filippo Manaigo

Academic Year 2018/2019

Abstract

Population models are used to determine the population densities of the excited states of an atom or a molecule given the plasma parameters. Such excited state densities are obtained by balancing the relevant excitation and de-excitation reactions included in the respective collisional radiative (CR) model which evaluates reaction balance by solving a set of coupled differential equations in the zero-dimensional approximation assuming steady states.

Such population densities depend on the parameters of the plasma, such as electron density and temperature. Thus, one field of application of population models is to determine plasma parameters by comparison with experimentally measured population densities (e.g. from optical emission spectroscopy (OES) measurements).

There are two main methods for plasma parameter evaluation based on optical emission spectra analysis with collisional radiative models. The first one is based on the comparison between the absolute line emission intensities predicted by the model and experimentally measured. The second one is based on the analysis of the ratio between pairs of emission lines. These lines should be chosen in order to obtain a line ratio which is a monotonic function of electron density. The former method requires absolutely calibrated spectra and provides more precise plasma parameter determination. The latter can also be used with relatively calibrated spectra. This makes line ratio method the more commonly used since an absolute calibration can be hard to achieve.

The main goal of this thesis is the creation and development of a collisional radiative model for Ar^+, based on the flexible package Yacora, to be used as a diagnostic for the line of sight averaged electron density and temperature in a plasma. This zero-dimensional model should take into account also diffusion as a mean particle loss probability. The contribution of diffusion can be important depending on the plasma application especially for metastable states but is usually not included in the set of differential equations due to its non linearity on electron density.

As for Ar^+ the line ratio to be used is already known. The ratio between lines at 480.6 nm and at 488.0 nm, in the region $5 \times 10^{16}\,\mathrm{m}^{-3} < n_e < 5 \times 10^{18}\,\mathrm{m}^{-3}$ [1], is particularly suitable for measuring the line of sight averaged electron density, due to its sensitivity on electron density and the weak dependence on electron temperature.

The choice of the input database for such model is crucial since the errors of the model are directly correlated to the accuracy of the used input data. Starting point for the development of the Yacora based model is a data set from ADAS which includes excited states energy levels, average collision strength for electron collision excitation processes and Einstein coefficients for spontaneous photon emission.

The initial version of the Yacora collisional radiative model for Ar^+ was successfully validated by comparing it with an existing Ar^+ model provided by ADAS and based on the identical input data. Additional processes, such as diffusion, were included in a following step and their impact on the prediction of the model are discussed.

Finally, the Yacora collisional radiative model for Ar^+ is used to characterize Ar plasmas generated in the Planar Inductive Coupled Experiment (PlanICE), currently in operation at EPP (AG Experimentelle Plasmaphysik) in the Department of Physics of University of Augsburg, and in a HiPIMS facility, in operation at the Institute for Electrical Engineering and Plasma Technology of Ruhr-University in Bochum. Both the experiments are used as a benchmark in order to cover a wider plasma parameter range.

Since, for the PlanICE experiment, the plasma parameters to be determined with the new model were known via the Langmuir probe, such measurements provided a validation of Yacora Ar^+ collisional radiative model.

Contents

Chapter 1

Introduction

1.1 Atomic Structure

1.1.1 Single Electron

A first simplified model for the description of the behaviour of electrons bound to an atom was proposed by Niels Bohr. Such model was later improved by E. Schrödinger who introduced the new concept of wavefunctions.

According to Bohr's theory, electrons bound to an atom perform orbits around the nucleus. The energies of the electrons, as well as the shape of these orbits, are described by different quantum numbers.

The first of these quantum numbers, the "principal quantum number" n_i, was introduced by Niels Bohr, who based his theory on the following assumptions [2]:

- Electrons, in an atom, move in orbits around the nucleus due to electrostatic attraction.
- The orbits performed by electrons are circular.
- A discrete and finite number of stable orbits are allowed, and these correspond to stationary states.
- Electrons in stable orbits do not irradiate photons

As direct consequences of these assumptions, an electron could only have a discrete number of allowed energy levels E_n and of orbital angular momenta L_n, which are a function of the principal quantum number n_i of the bound electron. Bohr further postulated that radiation can be emitted or absorbed when a transition between two allowed stationary states is made by an electron. The frequency (ν) of the radiation depends on the energy difference between initial and final states, according to the following equation.

$$|E_f - E_i| = h\nu \tag{1.1}$$

where h is the Planck constant and E_f and E_i are the energies of the final and initial excited state respectively. Considering the equation of Coulomb force acting on the electron interacting with a nucleus of charge Ze, where Z is the number of protons and $e = 1.6 \times 10^{-19}\,\mathrm{C}$ is the absolute value of the charge of protons and electrons, and the postulate on orbital angular momentum, the following system of equation can be obtained.

$$\begin{cases} \frac{Ze^2}{(4\pi\epsilon_0)r^2} = \frac{mv^2}{r} \\ L = mvr = n_i\hbar \end{cases} \tag{1.2}$$

where $\hbar = \frac{h}{2\pi}$ is the reduced Planck constant. The kinetic energy of the electron in the orbit can be obtained as a function of the principal quantum number $n_i \in \mathbb{N}_+$ by evaluating v and r, which are the electron speed and the orbit radius respectively [2].

$$E_n = \frac{1}{2}mv^2 + \frac{Ze^2}{(4\pi\epsilon_0)r} = -\frac{m}{2\hbar^2}\left(\frac{Ze^2}{4\pi\epsilon_0}\right)^2 \frac{1}{n_i^2} \tag{1.3}$$

in atomic physics energies are usually measured in electron volts (eV) instead of Joules (J). The conversion between these two units can be performed by multiplying the energy expressed in J by the electron charge e.

$$1\,\mathrm{eV} = 1\,\mathrm{J} \cdot 1.6 \times 10^{-19} \tag{1.4}$$

the Planck relation (equation 1.1), together with the postulates by Bohr allowing quantized energy levels, only explains the observed photon wavelengths emitted by H atom. An example for such observed wavelengths is the Lyman series: photons emitted as a consequence of spontaneous electron energy transition into orbits with principal quantum number $n_i = 1$, or the Balmer series, for which the final state of the transition is characterized by $n_i = 2$.

The model was then improved by E. Schrödinger who suggested the description of a generic electron bound to an atom as a wave function $\Psi(\mathbf{r}, t)$. This wave function is the eigenfunction, with energy E as eigenstate, of the Hamiltonian $\mathcal{H}$ [2]

$$\mathcal{H}\Psi(\mathbf{r}, t) = E\Psi(\mathbf{r}, t) \tag{1.5}$$

$$\mathcal{H} = -\frac{\hbar^2}{2m}\nabla^2 - \frac{e^2}{4\pi\epsilon_0 r} \tag{1.6}$$

which is an approximate equation for the bound electron Hamiltonian. The structure shown in equation 1.5 is similar also for momentum operators (the Hamiltonian is an energy operator). In particular, the orbital angular momentum operator

$$\mathbf{L}_i = \mathbf{r}_i \times \mathbf{p}_i \tag{1.7}$$

which is a function of position and momentum operators, can be applied to $\Psi(\mathbf{r}, t)$[1] to obtain the orbital angular momentum eigenstate. This requires the introduction of the orbital quantum number l_i. The upper limit of the l_i quantum number is determined by the principal quantum number n_i ($l_i \in \mathbb{N}$, $l_i \leq n_i - 1$). The orbital angular momentum eigenvalue can then be written.

$$\hbar\sqrt{l_i(l_i+1)} \tag{1.8}$$

similarly, other quantum numbers are defined, such as spin quantum number s which parameterizes the intrinsic angular momentum of a given particle. The spin of a single electron is $s_i = \{-\frac{1}{2}\hbar; \frac{1}{2}\hbar\}$. The spin operator $\mathbf{S_i}$ eigenvalue is

$$\hbar\sqrt{s_i(s_i+1)} \tag{1.9}$$

from the orbital and spin quantum numbers l_i and s_i the total angular momentum quantum number j_i can be defined. Its operator $\mathbf{J}_i$ represent the sum of the orbital angular momentum $\mathbf{L}_i$ and the spin momentum $\mathbf{S}_i$ operators. Since these are vectors the quantum number j_i can assume different semi integer values [2].

$$j_i = \{|l_i - s_i|, |l_i - s_i| + 1, ...|l_i + s_i|\} \tag{1.10}$$

1.1.2 Multiple Electrons

For atoms with more than one electron, the Schrödinger equation 1.5 cannot be solved exactly and approximation methods must be used [2]. Momentum operators can still be defined and their eigenvalues can be evaluated on the approximated wave functions.

In light atoms (low number of protons Z), orbital angular momenta l_i strongly interact among themselves and combine to form a total orbital angular momentum L. The same happens with electron spins s_i, forming a total spin angular momentum S. A weaker interaction between the quantum numbers L and S is called spin-orbit (or "LS") coupling. This interaction is described by a total angular momentum J. These quantum numbers L, S, J describe the global momenta properties of the whole atom and have the same structure shown in equations 1.8 and 1.9.

$$L = \sum_{i=1}^{N} \mathbf{l}_i \tag{1.11}$$

[1] To be more precise, angular momentum operators are usually applied to spherical harmonics. With these harmonics it is possible to describe the angular behaviour of Schrödinger equation $\Psi(\mathbf{r}, t)$

$$S = \sum_{i=1}^{N} \mathbf{s}_i \tag{1.12}$$

$$J = \{|L - S|, |L - S| + 1, ...|L + S|\} \tag{1.13}$$

where the index i runs over all the electrons of the atom. As for their single-electron counterparts, the quantum number L must be an integer, and S, J must be integer or semi-integer.

In heavy atoms (high number of protons Z) the coupling between the orbital l_i and the spin s_i angular momenta of a single electron becomes the dominant interaction. Thus a correct description of the atom is obtained with the jj coupling, where the total angular momentum of the whole atom is defined as

$$J = \sum_{i=1}^{N} \mathbf{j}_i \tag{1.14}$$

for each of the defined quantum numbers, its projection on the z axis can be defined as an additional quantum number.

1.1.3 Spectroscopic Notation

The electric configuration of a single electron is identified via its principal and orbital quantum numbers n_i and l_i according to the following structure.

$$n_i l_i \tag{1.15}$$

where l_i is substituted by a letter according to table 1.1.

Table 1.1: Correspondence between the value of l_i and the letters used in the spectroscopic notation. Starting from "f", code letters go on alphabetically.

Value of l_i	0	1	2	3	4	5
Code letter	s	p	d	f	g	h

In figure 1.1, the trend for the electron energies associated with each configuration level is shown. The energy, in first approximation, is a function of the principal and the orbital quantum numbers n_i and l_i. The number of bars associated to each level is determined by the magnetic quantum number m_i. This quantum number represent the eigenvalue of the projection on the z axis of the operator and can assume integer values whose absolute value is, at most, equal to the orbital quantum number $\mathbf{L}_i$ ($m_i = -l_i, -l_i+1, ...l_i$). If no magnetic field is applied, the value of m_i does not affect the energy of the electron. In addition, as mentioned before, electrons have an intrinsic spin angular momentum quantum number s_i which can assume two opposite values. The Pauli principle

states that in the same atom, two electrons with the same quantum numbers (n_i, l_i, m_i, s_i) cannot exist. Thus, each bar of figure 1.1 can be populated by up to two electrons with opposite spin quantum numbers.

In order to take into account the number of electrons that can populate a configuration level with certain values of n_i and l_i, in addition to the notation shown in equation 1.15 the number w of electrons is explicitly written as in the following structure.

$$n_i l_i^w \tag{1.16}$$

where, if $w = 1$, the number of electrons is usually omitted. It should be mentioned that, due to the Pauli principle, a configuration level characterized by the principal and the orbital quantum numbers n_i and l_i can be populated by up to $w = 2(2l_i + 1)$ electrons.

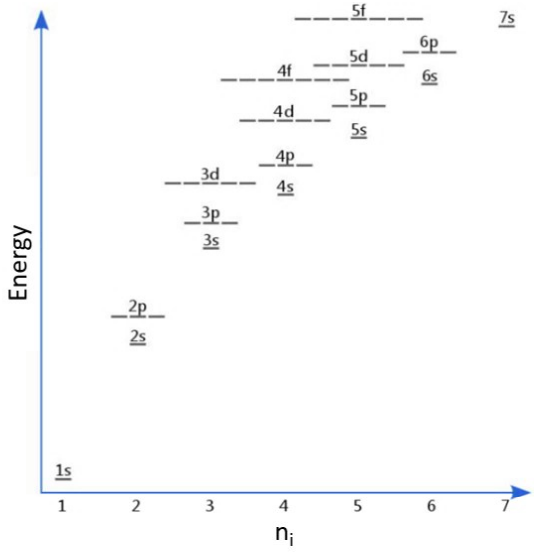

Figure 1.1: Quantum levels for electrons ordered by energy and quantum number n. Each line represents an energy level with fixed values of the quantum numbers n,l and m and can be populated by up to two electron with different spin quantum number [3]. Different lines with the same quantum numbers n and l do not have the same energy and are plotted together for simplicity sake.

As an example of a light atom, a Li atom in its ground state has two electrons at configuration 1s and one at 2s. Therefore it is written as.

$$1s^2 2s$$

Sometimes, if each possible configuration with a specific n_i or l_i is fully occupied, terms referring to electrons populating those configuration levels are

omitted, or substituted with an indication of the closest previous noble atom, as in the following examples for the same Li atom at ground state.

$$2s$$

$$[\mathrm{He}]2s$$

As mentioned before, if the LS coupling approximation can be used, the quantum numbers L and S identify the electrons of the atom as a whole. Thus a notation based on these quantum numbers is introduced[2].

$$(^{2S+1}L) \tag{1.17}$$

where the values of the orbital angular momentum L are substituted by capital code letters according to table 1.1, $2S+1$, which is a function of the spin angular momentum S, is called multiplicity.

Such notation does not take into account fine structure splitting, i.e. the energy differences between two states with different total angular momentum J. Energy differences due to the total angular momentum J are typically smaller than those due to the principal and the orbital quantum numbers n_i and l_i. States defined by the same L and S can differ by the z axis projection of such quantum numbers. Thus the state described only by the electron configuration (see equation 1.16) and the LS notation (see equation 1.17) groups $\widetilde{\omega}$ different degenerate states.

$$\widetilde{\omega} = (2S+1)(2L+1) \tag{1.18}$$

$\widetilde{\omega}$ is called "statistical factor".

If fine structure is taken into account, states with different J quantum number are no longer degenerate and the notation shown in equation 1.17 is expanded.

$$(^{2S+1}L_J) \tag{1.19}$$

the statistical factor ω associated with fine structure resolved states takes into account the different possibilities of the z axis projection of J (which, in the hyperfine structure introduces additional smaller energy differences).

$$\omega = 2J+1 \tag{1.20}$$

the $\widetilde{}$ is omitted to distinguish this statistical factor with one of a non fine structure resolved state.

As an example, the first excited Li state, with electrons in configuration $1s^2 2p$, is described according to the notation shown in equation 1.17 as

$$^2P$$

[2] A different notation can also be defined if the jj coupling approximation applies. This is not discussed in this thesis since for Ar^+ the LS coupling notation is used.

Due to the global electron quantum numbers of the Li atom $L = 1$, $S = \frac{1}{2}$, one can assume two different values of the total angular momentum $J = \frac{1}{2}$ or $J = \frac{3}{2}$. The difference between the energies associated to these two configurations can be neglected for this thesis purpose [4] since, in particular for atoms with a low number of protons and electron number.

$$\begin{cases} E(^2P_{\frac{3}{2}}) = 1.847\,818\,\text{eV} \\ E(^2P_{\frac{1}{2}}) = 1.847\,860\,\text{eV} \end{cases} \tag{1.21}$$

usually different excited states of the same atom can be characterized by the electrons occupying energetic level with the same n_i and l_i quantum number configuration. These two states cannot be distinguished by using only the notation shown in equation 1.16. This is because such notation does not provide information on how the spins and orbital angular momenta of the electrons in the same n_i and l_i level configuration are oriented with respect to each other. Thus, the notation to be used is a mix between what is shown in equations 1.16 (outside the brackets) which describes which configuration levels are occupied by electrons, and 1.19, which describes the L and S quantum numbers of the whole atom.

$$n_i l_i^w (^{2S+1}L_J) \tag{1.22}$$

Ar^+ Notation and Physics

Ar^+, the atomic species which this thesis focuses on, is a positive ion with 17 electrons and 18 protons ($Z = 18$). Its ionization energy (which is the second ionization of the neutral Ar atom) is 27.63 eV.

For an Ar^+ atom excited level, taking into account fine structure splitting implies corrections of the excited ion energies of, at most, 1 %. Therefore, for this thesis purpose, neglecting the quantum number J is still a good approximation when identifying the energies of the excited states of Ar^+ to be used. However, as it is shown in this thesis, the quantum number J has to be taken into account for a correct interpretation of the spectroscopic measurements since, the wavelengths of the emitted photons are sensible to the energy difference due to J.

The notation that is used to identify its excited levels is similar to the general case (see 1.22). An example of it is the following.

$$3p^4(^1D)3d(^2G)$$

The main difference is the presence of an "intermediate" L-S term (^1D) which, in the chosen example, has odd multiplicity and describes the "first" 16 electrons, excluding the one in $3d$ configuration. The second term (^2G), with an even multiplicity, takes into account all of the 17 electron of Ar^+. As mentioned before, configuration levels completely populated by $w = 2(2l_i + 1)$ electrons are not explicitly written.

Some noteworthy Ar^+ states are:

- $3p^5(^2P)$, the ground state
- $3p^6(^2S)$, the first excited state at 13.48 eV [4]
- $3p^4(^1D)3d(^2G)$, the metastable state[3] at 19.12 eV [4]

1.1.4 Selection Rules

Spontaneous emission is the transition from an excited state (with energy E_p) to a lower energy state (with energy E_q) that emits a single photon carrying the energy difference between the initial and final states.

$$\lambda_0 = \frac{c}{\nu} = \frac{hc}{E_p - E_q} \tag{1.23}$$

where: h is the Plank constant, c is the speed of light. The inverse process is the transition towards a higher energy state due to the absorption of a photon. Only photons whose wavelength corresponds to a possible transition can be absorbed.

The spontaneous emission probability (as well as photon absorption probability) per unit of time from the initial state p to the final state q is the Einstein coefficient A_{pq}, defined as follows in the dipole approximation[4]. The wavelength of the emitted photon is.

$$A_{pq} = \frac{(E_p - E_q)^3}{3\pi\epsilon_0\hbar^4c^3} |\langle p|\vec{d}|q\rangle|^2 \tag{1.24}$$

where $|p\rangle$ and $|q\rangle$ are the initial and final states respectively and $\vec{d} = -e\vec{r}$ is the dipole operator.

If the transition between the states p and q has $A_{pq} = 0$ such transition is optically forbidden. In order for the transition to be allowed, certain conditions (called "selection rules") have to be fulfilled. Within the electric dipole approximation only one unit of the total angular momentum can be carried by a photon. Thus, a transition is allowed only if the following selection rule is respected.

$$\begin{cases} \Delta J = 0, \pm 1 \\ (J_p, J_q) \neq (0, 0) \end{cases} \tag{1.25}$$

for completeness sake, in addition to this general rule there are two more conditions on the quantum number m ($\Delta m = 0, \pm 1$) and on the parity of the

[3] The definition can be found in section 1.1.4, where spontaneous emission is described.

[4] In such approximation the electromagnetic radiation wavelength is assumed to be much larger than the typical size of an atom. Thus the spatial part of the radiation field is approximated to $e^{i\vec{k}\cdot\vec{r}} \simeq i\vec{k}\cdot\vec{r}$, where $\vec{k}$ is the wavevector and $\vec{r}$ is the position in which the radiation is measured[5]

initial and the final state [4]. However, the database used in the creation of the Yacora Ar^+ model does not provide information about such quantities. Thus, these additional rules are not discussed in this thesis.

Spontaneous emission does not act on the electron spin variable. Thus, if the spin orbit coupling between the s_i and the l_i quantum number of a single electron can be neglected (so, if the LS coupling approximation described in section 1.1.2 is accurate), the following additional selection rules apply [6].

$$\begin{cases} \Delta S = 0 \\ \\ \Delta L = 0, \pm 1 \\ (L_p, L_q) \neq (0, 0) \end{cases} \tag{1.26}$$

unlike the rule stated in equation 1.25, these rules can be violated if the hypothesis assumed for the LS coupling atom description are not true.

This is the case of the Ar^+. For such ion, the LS coupling is used for naming the levels and the corresponding selection rules are valid for most optical transitions. Some exceptions exist like, for example, the spontaneous emission from $3p^4(^3P)3d(^4D)$, the second excited state, to $3p^5(^2P)$, the ground state. In such example the rule $\Delta S = 0$ is violated since the spin of the initial state is $S_p = \frac{1}{2}$ and the spin of the final state is $S_q = \frac{3}{2}$.

Excited states with no spontaneous emission transitions to lower energy states are defined as "metastable". An example of a metastable state is, for Ar^+, the state $3p^4(^1D)3d(^2G)$

1.2 Emission Spectroscopy

Spectroscopy is an indispensable diagnostic tool in astrophysics and plasma physics research. The collection and measurement of photons irradiated by particles in a plasma give plenty of real-time information on the observed plasma: both plasma processes and parameters, like electron density and temperature, can be studied with this tool. [7]

Two general spectroscopy techniques can be used: emission spectroscopy, which is a passive and non invasive method where the light spontaneously emitted by the plasma itself is measured, and absorption spectroscopy, where the light is provided by an external photon source pointed towards the detector. In the latter case, wavelengths corresponding to the energy difference between two states of the atoms and molecules composing the plasma may be attenuated depending on the parameters of the plasma itself. This occurs because photons of such wavelengths are absorbed by and excite the atoms or molecules of the plasma. Another photon, from the same particle, can then be emitted in a random direction. Most of them then do not reach the detector and, therefore, a weakening in the spectra of the corresponding wavelengths is observed.

Within the scope of this thesis emission spectroscopy is used. An example of a measured spectra, in the wavelength region between 480 nm and 489 nm, of an Ar plasma measured at the laboratory experiment PlanICE (discussed in section 2.1) is provided in figure 1.2 together with table 1.2.

The intensity I on the y axis corresponds to the number of photons per unit of time, volume and wavelength and is described by the following equation.

$$I(\lambda) = \frac{Signal(\lambda) \cdot CalibrationFactor(\lambda)}{ExposureTime \cdot PlasmaLength} \tag{1.27}$$

where $Signal$ is the actual output of the spectrometer. $ExposureTime$ is the time window of signal acquisition. $PlasmaLength$ is the length of the plasma section observed by the spectrometer. $CalibrationFactor$ is a factor which depends on the configuration of the spectrometer used.

A specific emission line is not an infinitely narrow line but is a Gaussian peak centered on the wavelength λ_0 corresponding to the energy gap of the transition, as it is shown in equation 1.23. Such broadening has several causes, the most relevant ones are [8]:

- Natural broadening, due to the Heisenberg uncertainty principle[5], which states that any given atomic energy level p does not have a perfectly defined energy E_p, but is rather a superposition of possible states spread. This implies that transitions between two energy levels do not correspond to an exact energy difference but show a distribution. The shape of such distribution is a Lorentzian[6].

- Thermal (Doppler) broadening, due to the fact that in a gas at kinetic temperature T, individual particles have random motions away from or towards the observer. The measured frequency ν_D, and consequently the photon wavelength, of a photon with frequency ν emitted from a particle moving with a velocity v towards the observer is

  $$\nu_D = \nu\left(1 + \frac{v}{c}\right)$$

  For a Maxwellian velocity distribution, the 1-D projected velocity distribution is Gaussian.

- Instrumental broadening, due to the used spectrometer

[5] $t \cdot \Delta E = h/(2\pi)$, where t is the time an electron occupies the higher energy state.

[6] The shape of a Lorentz distribution $\Psi(\nu)$ as a function of the photon frequency ν is

$$\Psi(\nu) = \frac{\Gamma}{4\pi^2(\nu - nu_0)^2 + (\Gamma/2)^2}$$

where Γ is the quantum-mechanical damping constant (the sum of all transition probabilities for natural decay from each of the lower and upper levels of the transition).

In order to evaluate the total number of photons (N_{ph}) generated by a specific spontaneous emission transition, the Gaussian peak centered at the corresponding wavelength has to be integrated. This, however, is only possible if an absolute calibration for the analyzed spectra is available and if the peaks in the spectra are actually detected as Gaussian by the detector.

$$N_{ph} = \int_{\lambda_k - \Delta\lambda}^{\lambda_k + \Delta\lambda} I(\lambda) d\lambda \tag{1.28}$$

where λ_k is the wavelength at the center of the Gaussian peak and $\Delta\lambda$ is an arbitrary interval that is usually chosen according to the width of the peak.

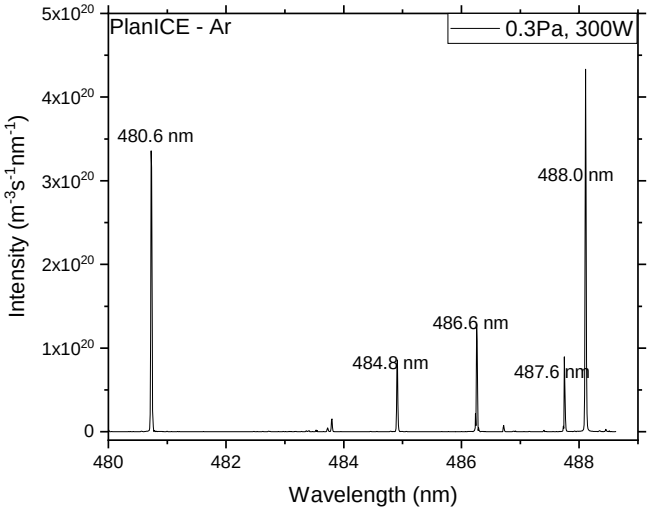

Figure 1.2: Ar plasma spectrum from PlanICE: it shows the number of measured photons per unit of time, volume and wavelength.

Usually optical emission spectroscopy (OES) is used, measuring wavelengths in the range between 300 nm and 1 μm. This range allows the measurements to be performed with relatively low experimental effort compared to wider ranges because, in the infrared (IR) range (wavelengths above 1 μm), thermal background noise becomes relevant and, in the ultraviolet/vacuum ultraviolet (UV/VUV) (below 300 nm), the air and the quartz glass are not transparent anymore. As for the OES measurement, an absolute calibration can be obtained with instruments like, as it is done in this thesis, an Ulbricht sphere (described in section 2.1.1).

The VUV range can be used to measure transitions directly linked to the ground state, which are called "resonant transitions" and typically involve a

Table 1.2: From left to right: the emitting species responsible for the transition, the transition wavelength, the upper state name, the upper state energy, the lower state name and the lower state energy of the lines labelled in figure 1.2

Atom	λ (nm)	Upper State	E (eV)	Lower State	E (eV)
Ar^+	480.6	$3p^4(^3P)4p(^4P_{5/2})$	19.22	$3p^4(^3P)3d(^4D_{5/2})$	16.64
Ar^+	484.8	$3p^4(^3P)4p(^4P_{1/2})$	19.22	$3p^4(^3P)3d(^4D_{3/2})$	16.64
Ar^+	486.6	$3p^4(^3P)5s(^4P_{3/2})$	22.51	$3p^4(^3P)4p(^4S_{3/2})$	19.97
Ar^+	487.6	$3p^4(^1S)3d(^2D_{3/2})$	22.31	$3p^4(^3P)4p(^2D_{3/2})$	19.76
Ar^+	488.0	$3p^4(^3P)4p(^2D_{5/2})$	19.68	$3p^4(^3P)4s(^2P_{3/2})$	17.14

higher energy gap between initial and final states of the transitions. However, all the measurements shown and analyzed in this thesis were acquired with OES.

1.3 Collisional Radiative Models

In order to interpret intensities measured by emission spectroscopy, a model describing the correlation between population densities of excited states with plasma parameters like the electron density (n_e) and, if the electron energy distribution function (EEDF) is Maxwellian, the electron temperature (T_e) can be used. Collisional Radiative (CR) models provide this description by balancing reactions that imply a change in the electron energy level of atoms or molecules in a plasma: the time derivative of the population density n_p of an excited state p can be written as a function of the other state densities [9].

$$\frac{dn_p}{dt} = \sum_{q>p} n_q A_{qp} - \sum_{q<p} n_p A_{pq} + n_e \left(\sum_{q \neq p} n_q X_{q \to p} - \sum_{q \neq p} n_p X_{p \to q} \right) \tag{1.29}$$

where n_e is the electron density, A_{qp} is the Einstein coefficient for the transition from state q to p, $X_{q \to p}$ is the rate coefficient for electron collision excitation (if $E_q < E_p$) and de-excitation (if $E_q > E_p$). This quantity describes, given an initial and a final state, the number of the considered electron collision processes per unit of time normalized by the densities of the colliding particles (i.e. the electron density n_e and the initial state density). If the plasma EEDF is Maxwellian, the rate coefficient for a generic electron collision process can be determined by integrating the product of velocity and cross section of such process over the velocity distribution.

$$X_{q \to p} = \langle \sigma(v) v \rangle_v = 4\pi \int_0^\infty \sigma(v) v^3 f(v) dv \tag{1.30}$$

electron collision is the main process with which excited states are populated. Its excitation rate coefficients depends on the EEDF, unlike the Einstein

coefficients associated to each spontaneous emission, which are fundamental constants.

However, in literature, instead of the cross section σ or to the rate coefficient $X_{q\to p}$, the collision strength Ω_{qp} is usually provided since it is a dimensionless quantity which is symmetrical between initial and final states [10]. Its relation with the cross section is.

$$\Omega_{qp}(\epsilon) = \widetilde{\omega}_q \left(\frac{E_q}{I_H}\right)\left(\frac{\sigma_{q\to p}(\epsilon)}{\pi a_0^2}\right) \tag{1.31}$$

where both Ω_{qp} and σ depend on the energy of the incident particle ϵ, $I_H = 13.6058\,\mathrm{eV}$ is the ionization energy of an H atom and $\pi a_0^2 = 8.7972 \times 10^{-17}\,\mathrm{cm}^2$ is a normalization for the cross section where the Bohr radius a_0 is used. Assuming a Maxwellian Electron Energy Distribution Function (EEDF) such quantity is then averaged.

$$\Upsilon_{qp} = \int_0^\infty \Omega_{qp}(\epsilon) \exp\left(-\frac{\epsilon}{k_b T_e}\right) d\left(\frac{\epsilon}{k_b T_e}\right) \tag{1.32}$$

the rate coefficient $X_{q\to p}$ can then be computed.

$$X_{q\to p} = \frac{2\sqrt{\pi}\alpha c a_0^2}{\widetilde{\omega}_q}\sqrt{\frac{I_H}{k_b T_e}} exp\left(\frac{\Delta E_{qp}}{k_b T_e}\right)\Upsilon_{qp} \tag{1.33}$$

where $2\sqrt{\pi}\alpha c a_0^2 = 2.1716 \times 10^{-8}\,\mathrm{cm^3 s^{-1}}$ is a constant which incorporates the fine structure constant and the Bohr radius, ΔE_{qp} is the threshold energy for the transition from state q to state p.

The inverse process $X_{p\to q}$ can be obtained using the detailed balance principle which states that: the ratio between the rates of the direct and the inverse processes is proportional to the ratio of the final state densities of the two processes [11]. The result is the following equation [12].

$$X_{p\to q} = \frac{\widetilde{\omega}_p}{\widetilde{\omega}_q} exp\left(\frac{\Delta E_{qp}}{k_b T_e}\right) X_{q\to p} \tag{1.34}$$

where the defined quantities are the same used in equation 1.33.

In equations 1.31, 1.33 and 1.34 $\widetilde{\omega}$ is substituted by ω if the considered states take into account fine structure splitting.

In equation 1.29, by taking $p = 1, ..., N$, where N is the total number of excited levels of the considered emitting particle specie, a whole set of coupled differential equations, describing the temporal evolution of the population density of each excited state, is obtained. Such set is a simplified example of a CR model which includes only the most relevant processes for a low pressure and low temperature plasma. However, it should be mentioned that such set of coupled differential equations neglects photon absorption. Phenomena like ionization or recombination can be included. The resulting population densities n_p of the excited state p can be written in terms of population coefficients.

$$R_{0p} = \frac{n_p}{n_0 \cdot n_e} \tag{1.35}$$

where n_0 is the ground state density and n_e is the electron density and, in general, n_p is a function of n_e.

This quantity can be plotted as a function of the electron density or temperature. It should be mentioned that, according to this definition, the population coefficient of the ground state n_0 is $R_{00} = n_e^{-1}$.

Different equilibria can be identified at low (approximately $n_e < 10^{15}\,\mathrm{m}^{-3}$ for Ar^+) and high (approximately $n_e > 10^{23}\,\mathrm{m}^{-3}$ for Ar^+) electron densities respectively[7].

- Corona equilibrium
- Local thermodynamic equilibrium

The behaviour of the population coefficient between the two regimes mentioned above cannot be predicted a priori and needs to be evaluated by CR models.

In the corona approximation regime, which holds for low electron density plasmas, since the thermal velocity of free electrons is low, fewer collision per unit of time are expected according to equation 1.30. In such condition $n_p \ll n_0$ can be assumed. This implies that the only relevant excitation contribution for a generic excited state p is the electron collision excitation process with ground state. For the same reason, electron collision de-excitation can be neglected and spontaneous emission becomes the main de-excitation process. Therefore the equation 1.29 becomes

$$\frac{dn_p}{dt} = -n_p \sum_{q<p} A_{pq} + n_e n_0 X_{0\to p} \tag{1.36}$$

with the following solution, in the steady state.

$$n_p = \frac{n_e n_0 X_{0\to p}}{\sum_{q<p} A_{pq}} \tag{1.37}$$

by using definition 1.35, a population coefficient independent of the electron density is obtained.

$$R_{0p}^{CM} = \frac{X_{0\to p}}{\sum_{q<p} A_{pq}} \tag{1.38}$$

as for metastable states, from which no spontaneous emission transition exists, the corona equilibrium cannot be reached if no additional loss term is included in equation 1.29. Thus particle diffusion, which is discussed in section 1.4, has to be included as a loss term in the CR model.

[7] Such values were identified using the simulations performed by Yacora Ar^+ model (see section 3.1.3).

With an increase in the electron density n_e, the density of the excited state n_p begin to deviate from the linear increase shown in equation 1.37. In the local thermodynamic equilibrium, high electron density regime, processes linear on electron density such as electron collision excitation and de-excitation become dominant. This leads to a saturation of a generic excited state density n_p and therefore the population coefficient assumes a $R_{0p} \propto n_e^{-1}$ behaviour. Excited states density of the emitting particle species follows the local Boltzmann distribution function [13].

1.4 Diffusion

Diffusion of particles in plasmas is a transport effect that, on average, moves particles from high to low density regions. Two main diffusion regimes can be distinguished according to the mean free path of the particles under investigation (an evaluation of the distance traveled, on average, by a particle between two consecutive interactions): either high or low collisionality.

The high collisionality regime usually holds for high pressure plasmas. The mean free path length is much smaller than the typical length of the plasma itself. The low collisionality regime holds instead in the opposite conditions. Both can be described with a confinement time, τ_d and τ_f, which describe the mean time required for a particle to be lost due to diffusion.

- Average confinement time τ_d: collisional diffusion regime.
- Free fall confinement time τ_f: collisionless diffusion regime.

The equations used for evaluating both confinement times are taken from a paper published by W. Möller el al. [14]. Once these two confinement times are evaluated, a total confinement time τ_t is obtained and its inverse is used as the probability of losing a particle of a specific excited state due to diffusion.

$$\tau_t = \tau_d + \tau_f \tag{1.39}$$

if the mean free path length is large compared to the container dimensions ("free fall" situation), the dominating confinement time is given by

$$\tau_f = \frac{\widetilde{\Lambda}}{v_a} \tag{1.40}$$

where v_a is the ambipolar velocity

$$v_a = \sqrt{\frac{2k_b T_e}{m_i}} \tag{1.41}$$

where m_i is the mass of the considered particle species and k_b is the Boltzmann constant. $\widetilde{\Lambda}$ is the average connection length from the place of production to the walls which, for a cylindrical container of radius ρ, in meters, is:

$$\widetilde{\Lambda} = \frac{\rho}{0.7722} \tag{1.42}$$

the used definition for the average confinement time τ_d neglects any magnetic field and, in order to obtain a simple solution, the sheath between the plasma and the wall. With these assumptions it can be written as:

$$\tau_d = \frac{\Lambda^2}{D_a} \tag{1.43}$$

where D_a is the ambipolar diffusion coefficient and Λ is the mean diffusion length. Its expression, given a cylindrical container of radius ρ and length $2l$, is:

$$\Lambda^2 = \left(\frac{8}{\rho^2} + \frac{3}{l^2}\right)^{-1} \tag{1.44}$$

where ρ and l are defined in meters.

Ambipolar diffusion D_a is related to mobility (μ_e, μ_i) and diffusion (D_e, D_i) of both electron and ions.

$$D_a = \frac{D_i\mu_e + D_e\mu_i}{\mu_e + \mu_i} = D_i + D_e\frac{\mu_i}{\mu_e} = D_i\left(1 + \frac{D_e}{D_i}\frac{\mu_i}{\mu_e}\right) \tag{1.45}$$

where $\mu_e \gg \mu_i$ was assumed. The ambipolar diffusion expression, together with Einstein relations,

$$D_i = \mu_i\frac{k_bT_i}{e}, D_e = \mu_e\frac{k_bT_e}{e} \tag{1.46}$$

can be modified in order be written as a function of ion mobility.

$$D_a = D_i\left(1 + \frac{T_e}{T_i}\right) = \mu_i\frac{k_b}{e}(T_i + T_e) \tag{1.47}$$

in order to evaluate this confinement time, the ambipolar diffusion coefficient have to be explicitly written as a function of the reduced mobility (μ_{red}) of an Ar^+ ion in a neutral Ar background gas. This quantity is usually tabulated since it is independent from gas conditions such as pressure and temperature and the relation between ion mobility μ_i and reduced mobility μ_{red} is described in the following equation:

$$\mu_{red} = \mu_i\left(\frac{p}{101\,325\,\mathrm{Pa}}\right)\left(\frac{273.15\,\mathrm{K}}{T_i}\right) \tag{1.48}$$

1.5 Plasma Parameter Evaluation

Population coefficients, predicted with CR models, are functions of plasma parameters, in particular of electron density n_e and temperature T_e. Therefore, CR models can be used to reproduce experimental measurements with plasma parameters as free parameters. Thus, joint application of spectroscopy and CR models offers a non invasive method of determining plasma parameters averaged over the spectrometer line of sight.

The value of n_e and T_e that better matches the experiment constitutes an estimation of these parameters. This fitting can be performed based on either:

- Absolute Line Emission
- Line Ratio R_{λ_k/λ_l}

Absolute Line Emission

Effective emission rate coefficients, for a specific wavelength λ_k, $X^{em}_{eff}(\lambda_k)$ describe the absolute number of photons with wavelength λ_k spontaneously emitted per unit volume and time and normalized by the ground state density n_0 and the electron density n_e. In order to obtain effective emission rate coefficients $X^{em}_{eff}(\lambda_k)$ the fraction of the population coefficient with the correct J quantum number has to be multiplied by the Einstein coefficient of the specific transition to be simulated:

$$X^{em}_{eff}(\lambda_k) = R_i \frac{\omega_k}{\sum_l \omega_l} A_{ij}(\lambda_k) \tag{1.49}$$

where R_i is the population coefficient of upper state i without fine structure splitting. The statistical factors, defined according to equation 1.20, would not be included in the equation if the population coefficient is referred to a fine structure split state.

From the effective emission rate coefficients evaluated with CR model, the absolute intensity (defined in equation 1.27) of a specific line can be computed according to the following equation.

$$I(\lambda_k) = n_e n_0 X^{em}_{eff}(\lambda_k) \tag{1.50}$$

where n_0 is the density of the ground state of the considered emitting particle species and n_e is the density of the electrons.

The prediction of the quantity $I(\lambda_k)$ can be compared with the observed emission lines (equation 1.27). This method can be used only if an absolute calibration of the measured spectra is available.

Line Ratio

Line ratio, between two different emission wavelengths λ_k and λ_l, R_{λ_k/λ_l} can be obtained by evaluating the ratio between effective emission rate coefficients.

$$R_{\lambda_k/\lambda_l} = \frac{X^{em}_{eff}(\lambda_k)}{X^{em}_{eff}(\lambda_l)} \tag{1.51}$$

the Line Ratio method only needs the analyzed spectra to have their lines relatively calibrated. This makes this method more viable since an absolute calibration is not easily achieved without a dedicated apparatus.

1.6 Ar plasma applications

Argon is chemical element whose atom is composed by 18 protons and is denoted with the symbol "Ar". It is one of the elements grouped as "noble" (also known as "inert") gases, which are characterized by their low reactivity. Such elements at standard conditions for temperature and pressure (273.15 K and 1×10^5 Pa) form odorless, colorless, monoatomic gases.

Argon is typically used as background gas for several plasma process and for surface processing.

Such processing is performed by exposing a surface to all the species and radiation that are produced in the plasma. Among them, the existing VUV photons have enough energy $> 6\,\text{eV}$ ($\lambda < 300\,\text{nm}$) to activate complex photochemical reactions which can change properties of the surface, e.g. breaking bonds in polymers [15]. As a consequence, quantification and even control of VUV photons became desirable in material processing applications [16].

In addition to surface processes that exploit the photons emitted from a plasma, sputtering is the ejection of particles from a solid surface bombarded by energetic particles of a plasma or gas. Once ejected, particles from the surface mix with those in the plasma or in the gas. This can compromise plasma purity and is usually a process to be avoided. However, there are several applications, such as precise etching and thin film layer deposition, in which sputtering is exploited.

Inert gases are usually employed as the sputtering gas because they tend not to react with the target material or to combine with any process gases and because they produce higher sputtering and deposition rates due to their large molecular weight [17].

Among inert gases, Ar is particularly used. Low ionization energy allow an easier plasma ignition since less energy is needed to generate ions and free electrons. Ar ionization energy (15.76 eV) is much lower than lighter noble elements (24.59 eV for He and 21.56 eV for Ne) and comparable to heavier noble elements (14.00 eV for Kr) which are more expensive. In addition to that an Ar plasma is relatively stable.

1.6.1 Sputtering Sources

The simplest layout of a sputtering apparatus is the DC powered diode, which is shown in figure 1.3. It consists in two planar electrodes, between which a

low pressure plasma is ignited. The target is placed on the cathode, where it is eroded due to collision with the incoming energetic ions produced in the plasma. Particles ejected from the target are then deposited by diffusion on a substrate which is usually placed on the anode and forms a thin film [18].

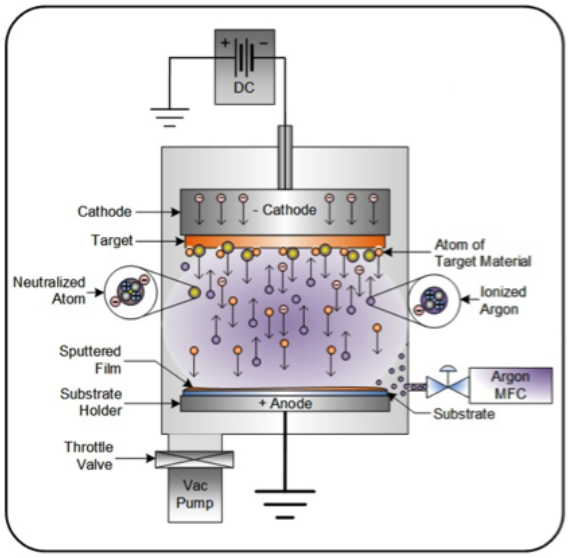

Figure 1.3: Scheme of a DC powered sputtering source in diode configuration. Pressure of the gas inside the chamber is regulated by the argon Mass Flow Controller (MFC) and by the vacuum pump [19].

Diode configuration proved not to be suitable for most application since the deposition rates are low (up to $0.1\,\mu$m/h for DC diode configuration [20]) at an optimal substrate temperature of $100 - 200\,^{\circ}$C. In order to improve the performances of sputtering applications, the use of magnetrons was introduced as shown in figure 1.4. Magnetrons or magnetron sputtering sources consist in permanent magnets located behind the cathode, where the sputtering target is placed. The magnetic field generated by such magnets traps the electrons and increases the frequency of electron collision, allowing the plasma to reach higher electron and ion densities in the proximity of the target. This improves sputtering and deposition rates (reaching up to $1\,\mu$m/h for DC magnetron configuration [20]) ensuring a low thermal load due to the reduced number of collisions between the energetic plasma ions and the substrate [18].

However, there are cases with DC magnetrons in which it is still not possible to obtain a long term stable process [18]. In order to further increase the performances of magnetron sputtering processes, the use of pulsed power supplies was introduced, in particular of High Power Impulse Magnetron Sputtering (HiPIMS). Such subclass of the magnetron sputtering method generates the plasma in short pulses, typically $10 - 100\,\mu$s, and with duty cicles, i.e. the duration of

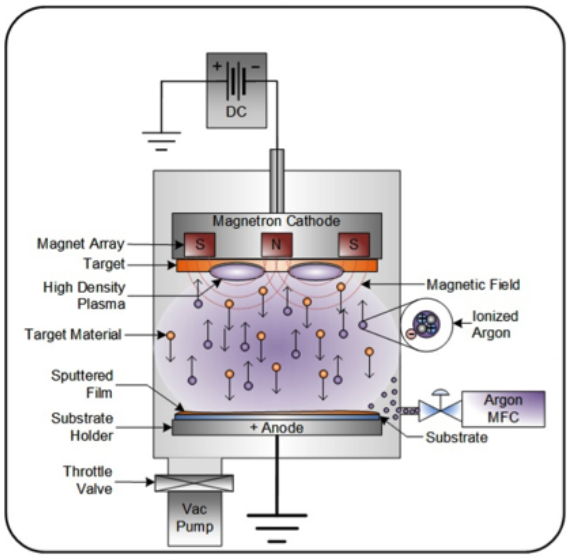

Figure 1.4: Scheme of the configuration shown in figure 1.3 with the addition of a magnetron [19].

the pulse with respect to the signal period, of about 1 %.

The use of a pulsed plasma is motivated by the possibility to use high power densities for short time intervals. This allows the plasma to reach higher electron densities, in comparison with the non pulsed method, while preventing the target from melting due to a too high energy deposition [21]. The deposition rate improves as well, reaching up to 5 μm/h for RF magnetron configuration [20].

1.6.2 Diagnostic Gas

Another application of argon is using it as a diagnostic gas in plasmas. As it is discussed in section 1.5, optical emission spectroscopy (OES) measurements can be used in order to evaluate the parameters, such as electron temperature and density, of the observed plasma.

For singly ionized argon, the ratio of the lines at 480.6 nm and 488.0 nm shown in figure 1.5, is particularly useful. Such line ratio has been chosen due to its sensitivity on electron density and the weak dependence on electron temperature in the region $5 \times 10^{16}\,\mathrm{m}^{-3} < n_e < 5 \times 10^{18}\,\mathrm{m}^{-3}$ [1]. This allows a rough estimation of the plasma electron density based on the measurement of this line ratio.

A small amount of argon can be added to other gas mixtures in order to exploit such property and obtain information on the electron density in the observed plasma from the ratio of the lines at 480.6 nm and 488.0 nm. This can

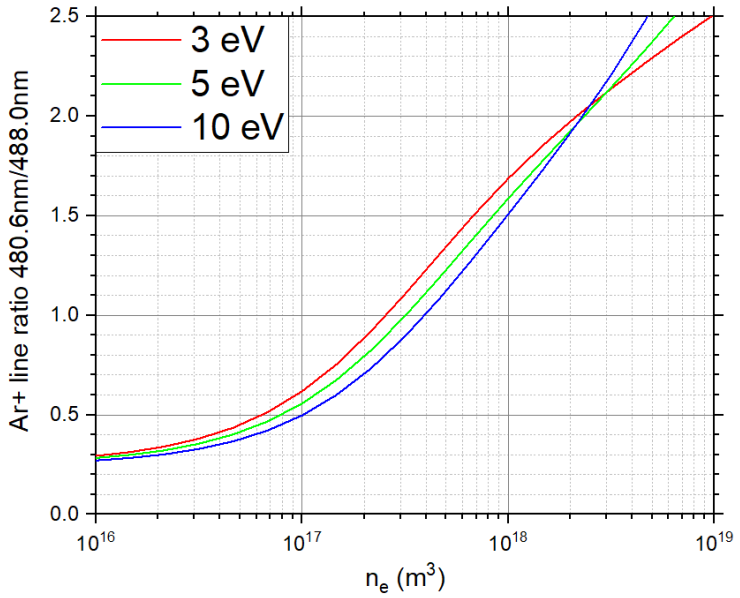

Figure 1.5: Line ratio of the Ar^+ lines at 480.6 nm and at 488.0 nm as a function of the electron density for three different values of electron temperature. These line ratio are calculated with Yacora, which is described in section 3.1.

only be done if the presence of argon does not imply changes in the key parameters of the generated plasma [7] and if the respective lines can be detected.

Chapter 2

Experimental Facilities

The experimental facilities from which the spectra used in this thesis were acquired are described in this chapter.

2.1 PlanICE

PlanICE (Planar Inductive Coupled Experiment) is a RF inductively coupled plasma source currently in operation at EPP (AG Experimentelle Plasmaphysik) in the Department of Physics of University of Augsburg.

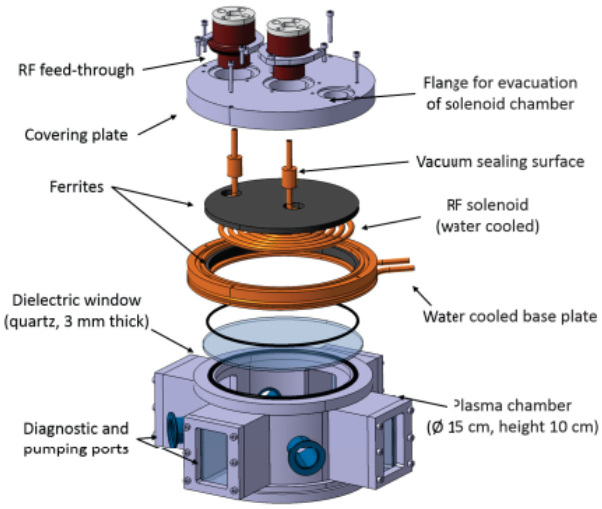

Figure 2.1: Schematics of PlanICE components [22].

An exploded drawing of PlanICE components is shown in figure 2.1. The plasma is generated by inductive coupling and confined in the plasma chamber: a stainless steel cylinder with 15 cm diameter and 10 cm height. Above the plasma chamber an antenna is placed: it consists in a copper solenoid insulated with teflon and surrounded by ferrites. The antenna is kept in vacuum and is separated from the plasma chamber by a 3 mm thick quartz window. The antenna is coupled to a RF generator which operates at 2 MHz and has a nominal maximum power of 2 kW [22].

The gas pressure can be regulated via the pumping ports located on its side and OES measurements can be performed through one of the four quartz windows. A photograph of the chamber with an Ar plasma inside is shown in figure 2.2. The produced plasma is stable in time: several measurements can be performed without plasma parameter changes.

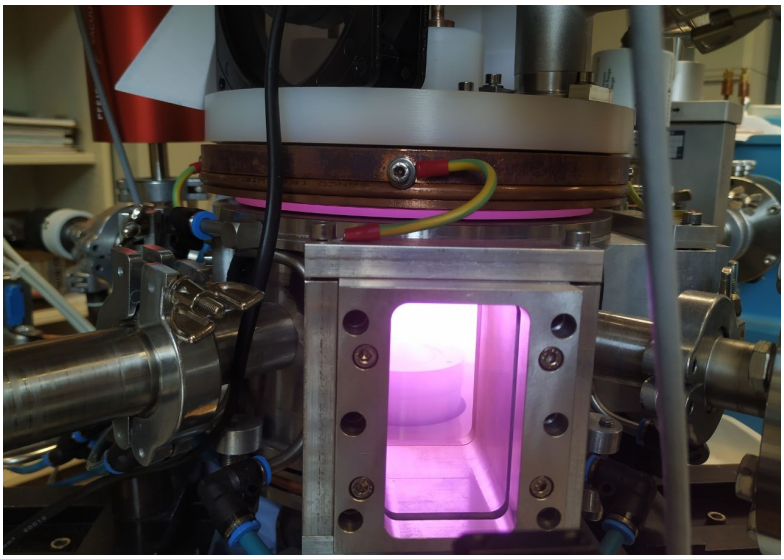

Figure 2.2: PlanICE operating with Ar plasma

A movable Langmuir probe is present in order to characterize plasma parameters such as T_e and n_e. It is placed on the side and it can move along the radius of the chamber.

The OES spectrometer is placed in front of the plasma chamber quartz window. Between them several filters could be placed in order to attenuate the light received. Neutral density filters were used for the acquisition of spectra with a wavelength range between 400 nm and 500 nm while a yellow filter was used for a wavelengths range between 500 nm and 520 nm. The spectral resolution of the OES spectrometer is of about 20 pm.

2.1.1 Calibration of the Optical System

In photometry experiments, especially for calibration purposes, it is common to measure the total luminous flux of a light source. This is done by measuring emission intensity at different angles and summing over them to determine the total flux.

A way of evaluating this quantity with a single measurement is to use an Ulbricht Sphere (also known as integrating sphere).

For the calibration of a spectrometer a light source, whose spectrum and absolute intensity are known, is placed inside a hollow sphere whose inner surface is covered by a highly reflective white coating. This causes multiple reflections of light within the sphere and, therefore, the inner surface to be uniformly illuminated [23]. Photons are then collected by the spectrometer to be calibrated through a small hole on the side of the sphere.

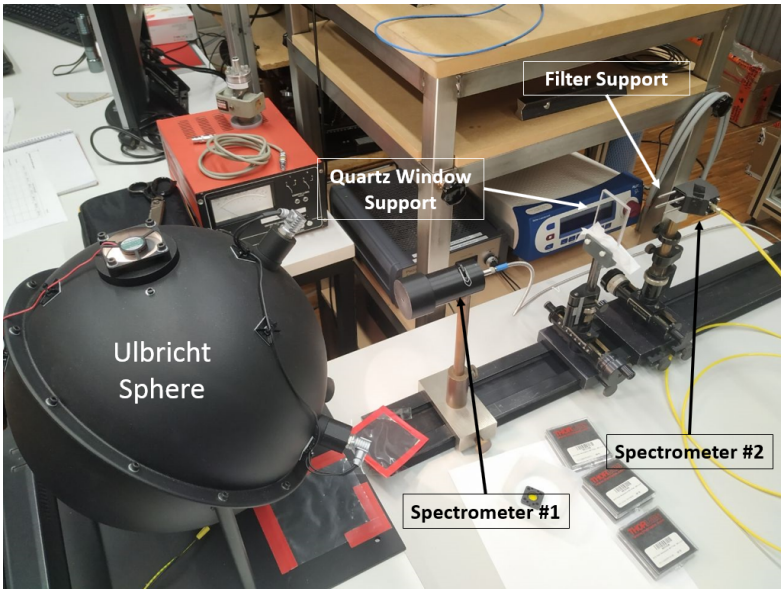

Figure 2.3: Ulbricht Sphere and two OES diagnostic seen from above.

Figure 2.3 shows, on the left hand side, the Ulbricht Sphere used for OES spectrometer calibration. The known light source is connected to a stabilized power supply. On the right hand side of the sphere, in order, the following objects can be seen:

- An OES spectrometer, labelled as "Spectrometer #1", only used for checking the heating of the lamp based on the emitted light. Such spectrometer can acquire full visible low resolution spectra several times per second, making it useful in order to control the emission of the sphere during the setup process. It was removed during the calibration.

- A support holding a quartz window of the same kind as those installed on the plasma chamber wall. It is kept between the sphere and the high resolution spectrometer ("Spectrometer #2") and it is used in order to take into account the attenuation due to the presence of the quartz window.

- The OES spectrometer used for the performed measurements, labelled as "Spectrometer #2". Attached to it there is a support for the filter used to attenuate the number of measured photons.

2.2 HiPIMS

As mentioned in section 1.6.1, Ar plasmas, produced by magnetrons, are widely used for sputtering and film deposition applications.

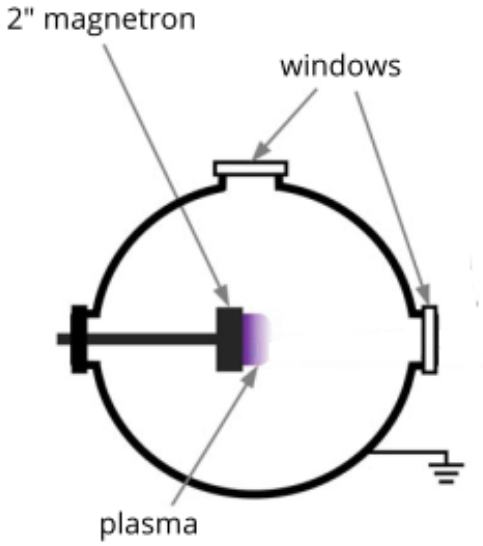

Figure 2.4: Scheme of the HiPIMS experiment currently in operation at the Institute for Experimental Physics II of Ruhr-University in Bochum [24].

Figure 2.4 shows the apparatus considered in this thesis, which is a High Power Impulse Magnetron Sputtering (HiPIMS) experiment. It is currently in operation at the Institute for Experimental Physics II of Ruhr-University in Bochum. It consists in a cylindrical plasma chamber with 40 cm diameter and 40 cm height.

Inside the plasma chamber a magnetron with 5 cm diameter target is mounted. The target is acting as a cathode, biased to about -500 V, accelerating positive

ions that sputter the target material. The typical average power is 100 W, while peak powers can be in kW range [25].

An Al solid target, where sputtering takes place, is located in the chamber, near the cathode. Discharges last for 200 μs and the impulse frequency is 10 Hz [26].

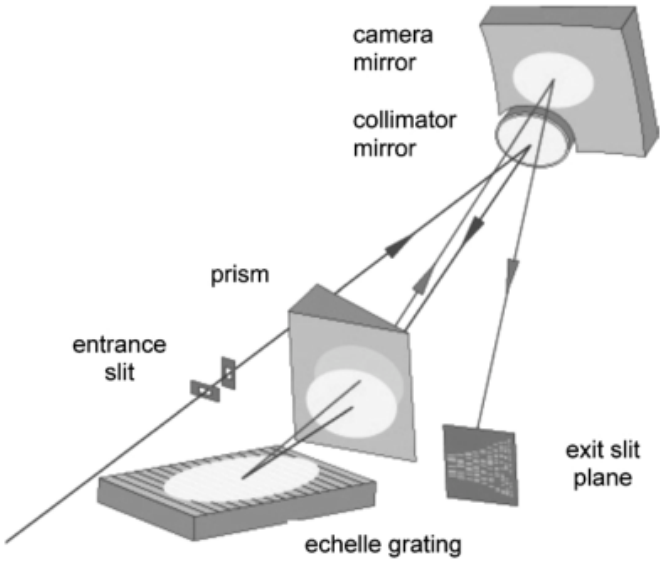

Figure 2.5: Scheme of the Echelle spectrometer used for the HiPIMS spectra measurements [27].

OES measurements are performed with a broadband Echelle spectrometer. This kind of spectrometers allow to obtain both high spectral resolutions and the possibility of simultaneously measuring spectra over ranges typically from 200 to 800 nm. A scheme of an Echelle spectrometer is shown in figure 2.5. An optical fiber transmits light to the spectrometers. Photons that pass through the entrance slit are redirected by a collimator mirror to a quartz prism.

The main difference between an Echelle and a standard spectrometer is the grating system. The prism is placed in front of such grating: the purpose of these two components is to deflect photons, according to their wavelengths, in two perpendicular directions. Spectrum is therefore recorded as a two-dimensional pattern which, after an additional reflection due to the camera mirror, is observed by a Charge-Coupled Device (CCD) detector [27].

The used Echelle spectrometer had a spectral resolution $\Delta\lambda = 30\,\text{pm}$ at 450 nm. It provided relatively calibrated spectra with a wavelength range between 200 nm and 800 nm [26].

Chapter 3

Ar^+ Collisional Radiative Model

3.1 Yacora

The flexible package Yacora [28] allows to solve the set of coupled ordinary differential equations (see equation 1.29) describing the gain and loss terms of the excited states of the described atomic or molecular species and thus determines the population coefficients for each of the excited state of the considered model. The collisional radiative models provided by Yacora are zero-dimensional. Thus transport processes like diffusion can be treated in an approximative way only and, therefore, can only be included as a mean particle loss probability.

Yacora allows non-linear (such as diffusion) and time-dependent effects to be implemented in the equations, which are integrated using the solver CVODE [29]. This is not possible when solving the set of coupled ordinary differential equations by matrix inversion.

The solver CVODE was chosen instead of solvers based on the Euler or Runge Kutta procedures. Such procedures choose a fixed time step according to the fastest reaction. This means that, if a reaction has a rate some order of magnitude lower than the fastest one, a lot of computational time can be consumed. CVODE, in contrast, uses the Backward Differentiation Formula (BDF) method for solving stiff equation systems. This method is based on a predictor-corrector scheme: a first-order approximation with a small time step is used at the beginning of the integration. During the integration process, the available information from previous time steps is applied in order to increase the time step and increase the simulation speed.

The definition of the model to be solved, i.e. the description of the set of coupled ordinary differential equations, is implemented in Yacora via a text file. Once, in this file, all the species and excited states are named, the probabilities for all the reactions have to be defined: for example, the probabilities for

collisional processes are evaluated from either rate coefficients or cross sections. The definition of additional reaction probabilities can be based on user defined variables. These user introduced terms are then included in the set of coupled differential equations that Yacora integrates. The reaction probabilities (i.e. cross sections and transition probabilities) related to the individual processes are usually not modified once the model is benchmarked, unless more accurate data are available.

Plasma parameters, such as electron temperature and density and initial density of one or more particular states, are defined in an additional text file, together with the user defined input parameters used in the file containing the description of the reaction probabilities.

At the end of the simulation Yacora can give as output population coefficients (see definition 1.35) for the chosen plasma conditions. If needed, additionally the time trace of each state density, as a function of the time of the simulation, can be written. Finally, also the balance which shows the contributions of all exciting and de-exciting reactions, in term of reaction rates, for a specific state in equilibrium can be obtained.

The goal of this first version of the Yacora Ar^+ model (which in the graphs is referred as "Yacora v1") is to be able to replicate the results of ADAS, a software which can provide collisional radiative models for several different plasmas. Thus, the processes included and described in section 3.1 are those used in the model by ADAS. ADAS itself, as well as the comparison between its results for Ar^+ and those of the first version of the Yacora Ar^+ model, are discussed in section 3.2.

3.1.1 Ar^+ Model Input Data

Cross sections, from which electron collision excitation rate coefficient were evaluated, were obtained by D. C. Griffin et al. in 2007 [30] from a 452-state RMPS (R-Matrix with Pseudo States) close-coupling calculation. The corresponding Maxwellian averaged collision strengths (Υ_{ij}), are available in the Open-ADAS database [31] as "resolved specific ion data collections". This kind of database includes:

- a list of energy levels, each one labelled with an index.
- averaged collision strength (Υ_{ij}), as a function of electron temperature, for the electron collision excitation between each states.
- spontaneous emission Einstein coefficients between each states.

The levels included, shown in figure 3.1 and listed in table 3.1 (together with a list number that, from now on, is used to help with the identification of the excited states included in the Griffin 2007 calculations), are the 40 lowest energy states of the argon ion. The considered states do not take into account fine structure splitting, whose effects are implemented later in the analysis of

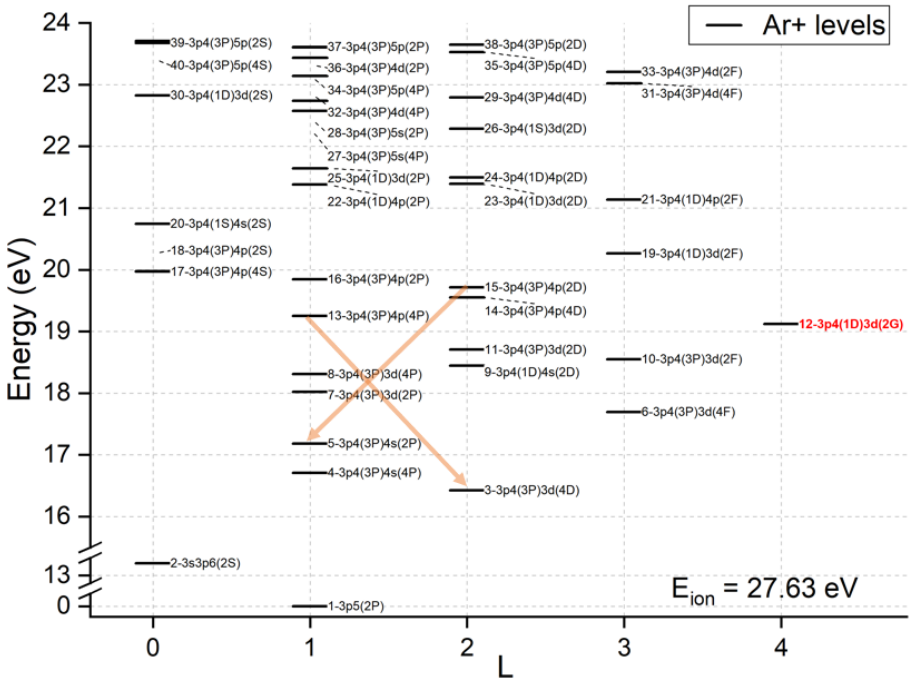

Figure 3.1: Ar^+ energy levels according to D. C. Griffin et al. 2007 [30]: The state labelled in red is the metastable one.

Yacora output files, discussed in section 3.1.3. The number of sub levels in which each of the considered 40 Ar^+ states is divided if fine structure is taken into account is listed in the table. An important quantity associated to each state is its statistical factor which is determined by the spin quantum number S and the azimuthal quantum number L according to the equation 1.18. In addition, also the mean lifetime of the state, which is evaluated as the inverse of the sum of each of the Einstein coefficients from the same state, is considered.

$$\tau = \frac{1}{\sum_j A_{ij}} \tag{3.1}$$

the ground state is $1-3p^5(^2P)$. The state $12-3p^4(^1D)3d(^2G)$ is metastable, which, as mentioned before, means that it cannot decay via spontaneous emission to any energetically lower state and hence has a long life time. Due to this, for low collisionality (i.e. low electron density) the loss of particles due to diffusion becomes the predominant loss process in the differential equation for a metastable state. It has to be ensured that the relevant excitation channels are considered for this state. For low collisionality the diffusion of the metastable state (although to be implemented in a zero-dimensional model only in an ap-

proximative way) is included in the Yacora Ar$^+$ model introduced in section 3.3.

Table 3.1: Energy ordered list of the Ar$^+$ state included in D. C. Griffin (2007) data set [30]. From left to right: the list number associated to each state, the name of the state, its energy, the statistical factor $\widetilde{\omega}_i$ associated to the non resolved state, the number of sublevels in which the state splits if fine structure is taken into account and the mean lifetime associated to that state. Stable states are marked with their number and name in bold.

#	Spectroscopic Notation	Energy (eV)	$\widetilde{\omega}_i$	Sublevels	τ (s)
1	$\mathbf{3p^5(^2P)}$	0	6	2	
2	$3s^3p^6(^2S)$	13.490	2	1	8.47×10^{-9}
3	$3p^4(^3P)3d(^4D)$	16.437	20	4	1.86×10^{-5}
4	$3p^4(^3P)4s(^4P)$	16.720	12	3	2.13×10^{-7}
5	$3p^4(^3P)4s(^2P)$	17.195	6	2	2.74×10^{-10}
6	$3p^4(^3P)3d(^4F)$	17.707	28	4	3.41×10^{-6}
7	$3p^4(^3P)3d(^2P)$	18.034	6	2	1.51×10^{-6}
8	$3p^4(^3P)3d(^4P)$	18.320	12	3	3.24×10^{-7}
9	$3p^4(^1D)4s(^2D)$	18.457	10	2	3.27×10^{-9}
10	$3p^4(^3P)3d(^2F)$	18.562	14	2	1.02×10^{-7}
11	$3p^4(^3P)3d(^2D)$	18.716	10	2	4.57×10^{-10}
12	$\mathbf{3p^4(^1D)3d(^2G)}$	19.132	18	2	
13	$3p^4(^3P)4p(^4P)$	19.264	12	3	7.37×10^{-9}
14	$3p^4(^3P)4p(^4D)$	19.564	20	4	7.29×10^{-9}
15	$3p^4(^3P)4p(^2D)$	19.728	10	2	9.71×10^{-9}
16	$3p^4(^3P)4p(^2P)$	19.860	6	2	8.13×10^{-9}
17	$3p^4(^3P)4p(^4S)$	19.983	4	1	5.41×10^{-9}
18	$3p^4(^3P)4p(^2S)$	19.988	2	1	7.35×10^{-9}
19	$3p^4(^1D)3d(^2F)$	20.277	14	2	1.10×10^{-5}
20	$3p^4(^1S)4s(^2S)$	20.760	2	1	1.72×10^{-10}
21	$3p^4(^1D)4p(^2F)$	21.153	14	2	6.94×10^{-9}
22	$3p^4(^1D)4p(^2P)$	21.393	6	1	4.26×10^{-9}
23	$3p^4(^1D)3d(^2D)$	21.408	10	1	1.45×10^{-10}
24	$3p^4(^1D)4p(^2D)$	21.512	10	2	6.09×10^{-9}
25	$3p^4(^1D)3d(^2P)$	21.658	6	2	1.34×10^{-10}
26	$3p^4(^1S)3d(^2D)$	22.301	10	2	1.22×10^{-9}
27	$3p^4(^3P)5s(^4P)$	22.586	12	3	7.28×10^{-9}
28	$3p^4(^3P)5s(^2P)$	22.752	6	1	1.33×10^{-9}
29	$3p^4(^3P)4d(^4D)$	22.809	20	2	3.12×10^{-9}
30	$3p^4(^1D)3d(^2S)$	22.842	2	1	1.85×10^{-10}
31	$3p^4(^3P)4d(^4F)$	23.033	28	3	3.63×10^{-9}
32	$3p^4(^3P)4d(^4P)$	23.157	12	1	4.09×10^{-9}
33	$3p^4(^3P)4d(^2F)$	23.221	14	1	4.86×10^{-9}

Continued on next page

#	Spectroscopic Notation	Energy (eV)	$\widetilde{\omega}_i$	Sublevels	τ (s)
34	$3p^4(^3P)5p(^4P)$	23.447	12	2	3.58×10^{-8}
35	$3p^4(^3P)5p(^4D)$	23.545	20	1	3.08×10^{-8}
36	$3p^4(^3P)4d(^2P)$	23.621	6	1	1.86×10^{-10}
37	$3p^4(^3P)5p(^2P)$	23.625	6	2	1.01×10^{-8}
38	$3p^4(^3P)5p(^2D)$	23.664	10	1	1.97×10^{-8}
39	$3p^4(^3P)5p(^2S)$	23.692	2	1	1.53×10^{-8}
40	$3p^4(^3P)5p(^4S)$	23.720	4	1	2.23×10^{-8}

Other data sets from Open-ADAS, for Ar^+ electron collision excitation cross sections, have also been checked. Such data sets contained estimations on the same physical quantities, previously listed, described in the used data set for a different number of states and with a different precision. The additional data sets shown as an example are:

- the set by D. C. Griffin et al. (1997) [12] based on a 43-term (instead of the more precise 452-term of his data published on 2007) RPMS calculation. States with an electron on an $n_i = 5$ orbit are not considered.
- the set by M. O'Mullane et al. (1994) [31], whose calculations are based on a different method (Hartree-Fock method). Some of its predicted energy levels differs by a 10 % with respect to the NIST Database.

Between those with a comparable amount of states, the one by D. C. Griffin et al. (2007) is the one with most base functions included in RMPS calculations and, therefore, is assumed to be the most accurate. In agreement with this assumption, figure 3.2 shows the comparison between energies of excited Ar^+ levels from three different sets of data and measured values available on NIST database [4]. Thus, the D. C. Griffin et al. (2007) data set was chosen as initial point for constructing the Yacora Ar^+ model.

3.1.2 Input Data Processing

Once the database to work with has been chosen, using equation 1.33, the average collisional strengths Υ_{ij} are converted into the rate coefficients ($X_{i\to j}$) in order to be processed by Yacora.

For each transition, the input file taken from Open-ADAS provides Υ_{ij} values for eight different electron temperatures ranging from 0.3 eV to 70 eV (approximately one point for each temperature increase of a factor of 2). Therefore the same number of interpolation values of $X_{i\to j}$ is available. Yacora performs a fit on these input rate coefficients. Such fit assumes a straight line from each point to the consecutive one. Thus, such number of input points in not sufficient. When using Yacora for calculating population coefficients, based on the eight interpolation values of $X_{i\to j}$ from Open-ADAS, a log-log plot of the

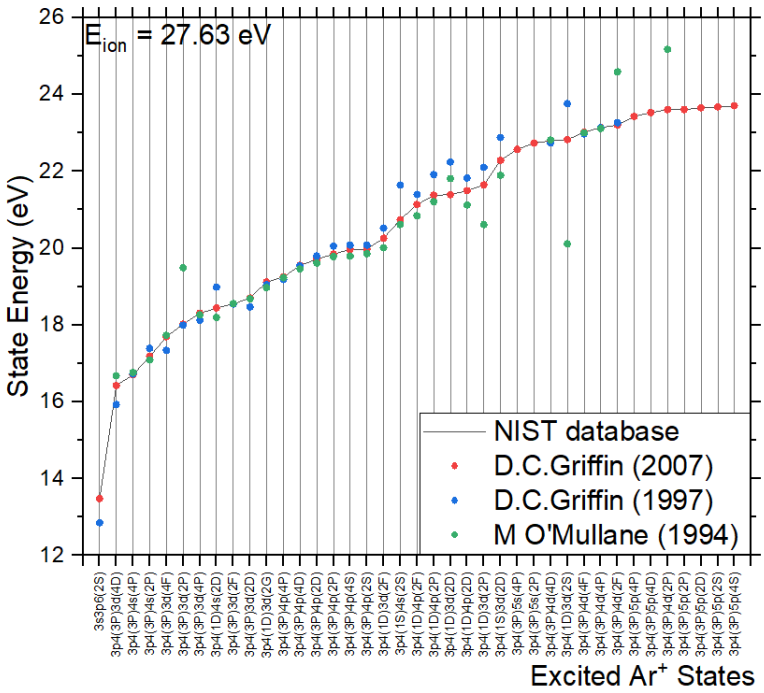

Figure 3.2: Ar$^+$ energy levels comparison between three different sets.

result, see the left part of figure 3.3, shows a non expected behaviour in the interval between two consecutive input points. The population coefficients at the electron temperatures corresponding to the available input rate coefficients are labelled as "Original Ar$^+$ Input Points" and the line interpolating them are the straight connections which look like curves in a log-log plot.

In order to obtain a smoother function for each population coefficient, more points are needed. Thus, a fit was performed on the eight interpolation values of the original input rate coefficients. An arbitrary number of points could then be chosen from the fit function and new, more populated, input files were generated with a hundred of points.

The fitting function was chosen according to Janev suggestion [32] which, for a generic electron collision process, parametrizes the logarithm of the rate coefficient as a power series of the logarithm of the electron temperature.

$$lnX_{i\to j} = \sum_{n=0}^{k} b_n \big(lnT_e\big)^n \tag{3.2}$$

where b_n are the polynomial coefficients. Logarithms are chosen since both the rate coefficients and the electron temperature can vary of several orders of magnitude. The suggested upper limit of $k = 8$, corresponding to 9 degrees of

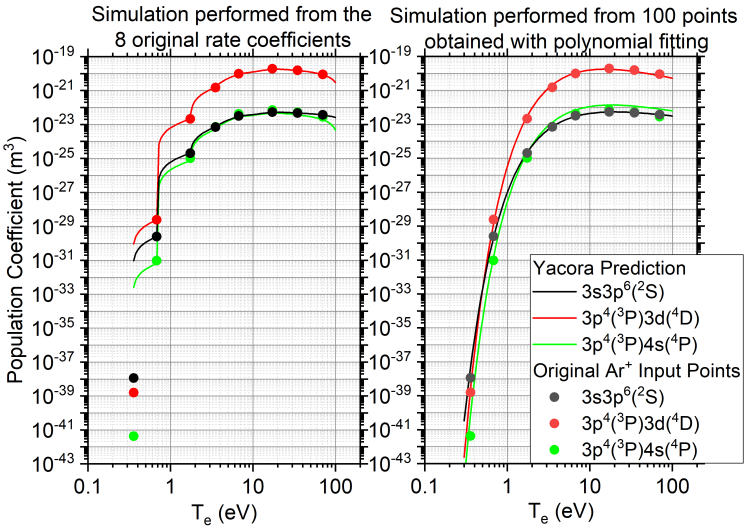

Figure 3.3: Left: Population coefficients from Yacora. As input the 8 available rate coefficients interpolation values (obtained from the corresponding Υ) were used. Right: The same population coefficients but with more interpolation values for the input rate coefficients which were obtained with a polynomial fitting.

freedom of the function, could not be imposed since the points available to be fitted are 8. $k = 7$ was used instead.

Before applying such fitting procedure to the Ar^+ excitation rate coefficients from Open-ADAS, its goodness was tested. The electron collision rate coefficients with He atoms, taken from a paper by T. Fujimoto [33], was considered since they were used as input in an already existing and benchmarked Yacora CR model. Fujimoto's article provided to such Yacora He model a sufficient number of interpolation values (~ 100) for each electron collision processes and the issue shown on the left-hand side of figure 3.3 was not present. The number of these input points was artificially reduced to eight by choosing the rate coefficients at the same electron temperature available for the Ar^+ input database. For several electron collision processes such eight input points were fitted using the fitting function 3.2. Figure 3.4 shows an example for the electron collision ionization from the He (3^1P) excited state, which is characterized by an energy of 23.09 eV. He has an ionization energy of 25.6 eV. The upper part of figure 3.4 shows the fit performed on the points marked in red. The other points, not used in the fit coefficients determination, are also shown in order to compare the fit function behaviour with what it should simulate.

With the exeption of temperatures outside the interpolation range, the fitting function described with equation 3.2 well reproduces the behaviour of the

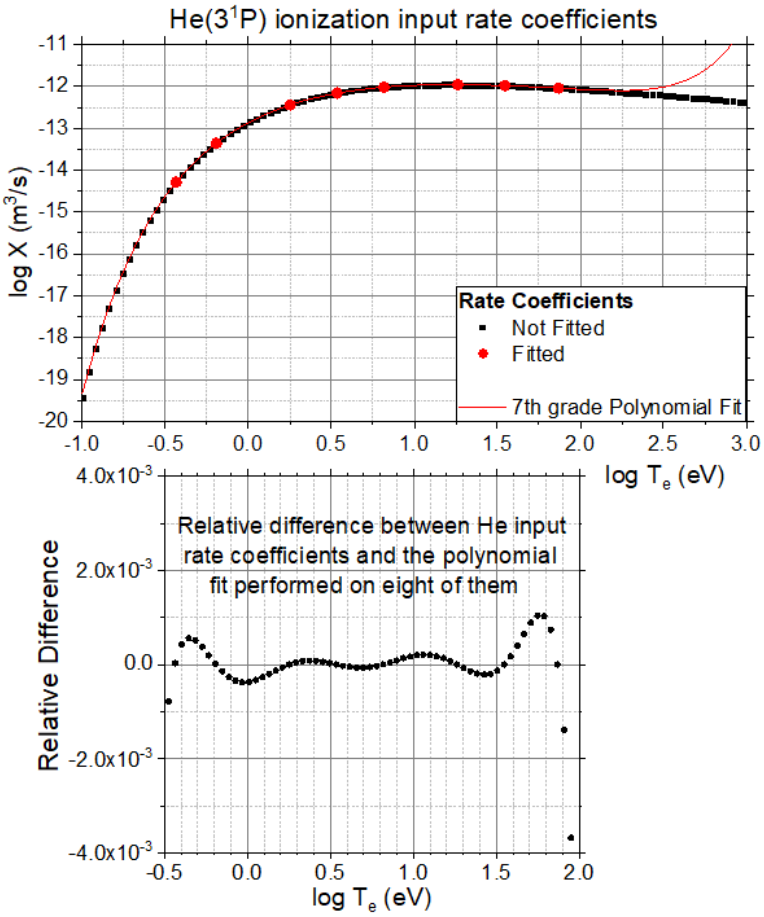

Figure 3.4: Top: logarithm of the rate coefficient of He (3^1P) electron collision ionization transition together with the fit described with equation 3.2. The fit was performed on the eight red points. Bottom: relative residuals between the absolute values of rate coefficients obtained from the fit and from the transition input files. This difference was then normalized on the latter one.

physically measured rate coefficients with errors of, at most, few per mille. This is confirmed by the residual plot in the bottom part of figure 3.4 The same was observed for several other electron collision processes for He, thus the fitting function is assumed to be consistent in the region between the available input rate coefficients and can be used for the Ar^+ input rate coefficients.

Applying the same type of fit to the Ar^+ input rate coefficients allowed to obtain a smoother prediction by the solver, as shown on the right hand side graph in figure 3.3.

Electron collision de-excitation is taken into account by using equation 1.34 with the rate coefficients obtained with the fitting procedure.

To summarize, the states and processes included in this first version of Yacora Ar^+ model are the following.

- The 40 Ar^+ states with lowest energy, without taking into account fine structure splitting.
- Electron collision excitation between each of the implemented excited states mentioned above.
- Electron collision de-excitation between each of the implemented excited states mentioned above.
- Spontaneous emission.

The rate coefficients and Einstein coefficients for these processes have been taken from the data provided by D. C. Griffin in 2007 [30], available in the Open-ADAS database [31]. As mentioned earlier this database, as well as each of the databases found in Open-ADAS for Ar^+, contains quantities which can be defined only if the EEDF is Maxwellian. This limits the applicability of Yacora CR Ar^+ model.

No other process was included in the first version of the Ar^+ Yacora model since those listed above are the processes taken into account by ADAS model discussed in section 3.2 and, as mentioned before, the goal of this first version is to reproduce ADAS results.

3.1.3 Output Data Processing

As already mentioned, Yacora can provide population coefficients, as a function of electron density or temperature, for each excited state present in the model. Figure 3.5 shows, as an example, for a wide range of the electron density the population coefficient of three states of the Ar^+ ion. The electron temperature was set to 3 eV. The state $2-3s3p^6(^2S)$ was chosen because it is the first excited state of the Ar^+ ion, while states $13-3p^4(^3P)4p(^4P)$ and $15-3p^4(^3P)4p(^2D)$ are shown because they are the upper states of emission lines at 480.6 nm and 488.0 nm, which as mentioned in section 1.6.2 can be used for the determination of the electron density of the plasma. Figure 3.5 does not show the population coefficient of the ground state $R_{00} = n_e^{-1}$ which, for an electron temperature of 3 eV, in the local thermal equilibrium region (the region in which is closer to the other population coefficients), is a factor of ~ 200 higher than the population coefficient of the first excited state $2-3s3p^6(^2S)$.

As discussed in section 1.3, corona model and thermal equilibrium region can be distinguished for lower (approximately $< 10^{15}\,m^{-3}$) and higher (approximately $> 10^{23}\,m^{-3}$) electron densities, respectively. As expected, the simulation shows, for the population coefficients of each of the states, a constant behaviour

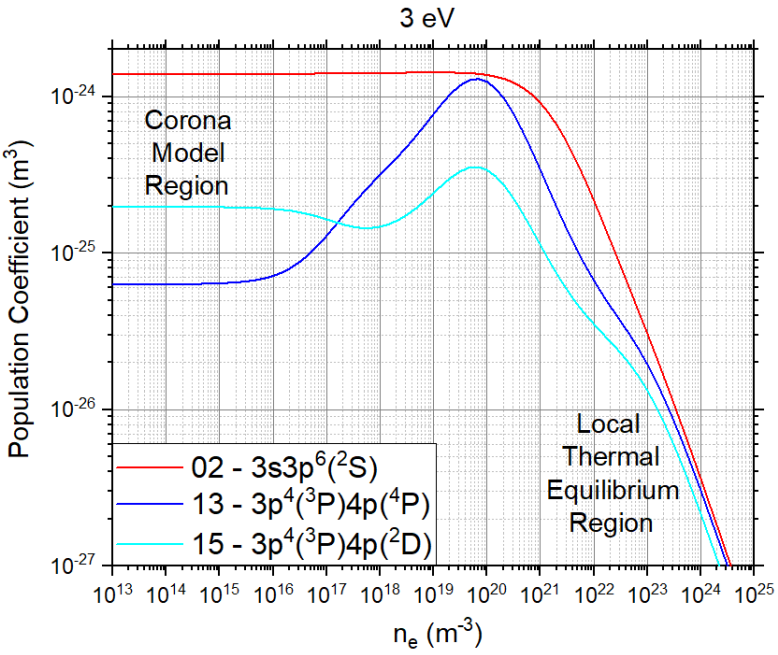

Figure 3.5: Population coefficient of three excited states as a function of electron density for an electron temperature of 3 eV. The first two digit index refers to the number associated in table 3.1 to each state.

in the corona model region and the n_e^{-1} dependency in the local thermal equilibrium region. In between the two regions very different behaviour can be observed. As an example, state $13 - 3p^4(^3P)4p(^4P)$ shows an increase of the population coefficient from an electron density of $1 \times 10^{16}\,\mathrm{m}^3$. This happens because the density of the excited states (not to be confused with the population coefficient, their relation is stated in equation 1.35) is increasing and electron collision excitation from lower excited states becomes more important than excitation from ground state. The same effect is not seen for the state $2-3s3p^6(^2S)$ since that is the first excited Ar^+ state and thus, the only electron collision excitation process with $2 - 3s3p^6(^2S)$ as the final state is from the ground state. A maximimum of the population coefficient for states $13 - 3p^4(^3P)4p(^4P)$ and $15-3p^4(^3P)4p(^2D)$) is reached around an electron density of $1 \times 10^{20}\,\mathrm{m}^3$, where the effect of electron collision de-excitation begins to balance the excitation processes.

From the non fine structure resolved population coefficients, the effective emission rate coefficients are obtained using equation 1.49.

As already mentioned, the Einstein coefficients provided in the input database describe the spontaneous emission transition between states that do not take

into account the fine structure splitting. The resolved Einstein coefficients for specific lines $A_{ij}(\lambda_k)$ are available from the NIST Database [4]. Figure 3.6 shows a scheme of how fine structure splitting plays a role in the determination of lines 480.6 nm and 488.0 nm, which are the lines mostly used in the model analysis. Tables 3.2 and 3.3 show the quantities needed for the fine structure splitting effect evaluation for each of the spontaneous emission transitions with the same initial and final Ar^+ state.

The fine structure resolved states, labelled with the corresponding J quantum number, are colored according to the name of the corresponding non fine structure resolved state. The red arrows indicate the emission lines mentioned above highlighting initial and final states and the Einstein coefficients for that transition.

An example of the resulting effective emission rate coefficient, as a function of electron density for two different electron temperatures, is shown in figures 3.7 and 3.8. For completeness sake, figure 3.9 shows the effective emission rate coefficient as a function of the electron temperature.

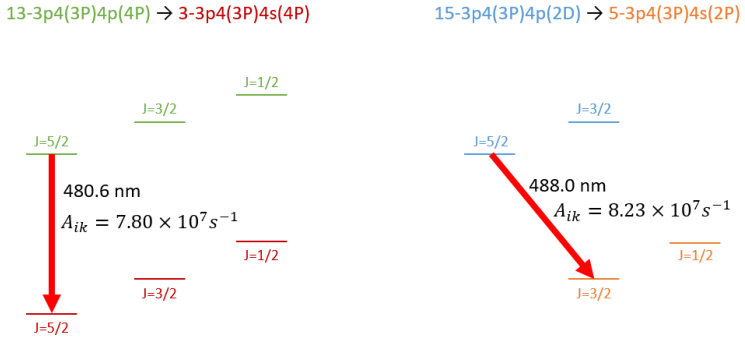

Figure 3.6: Example of fine structure splitting scheme. The statistical weight of the fine structure resolved states is $\omega = (2J + 1)$

Using these two lines, the ratio between 480.6 nm and 488.0 nm rate coefficient was evaluated and it is shown in figure 3.10. As described in section 1.6.2, this line ratio is used due to its sensitivity on electron density and to the weak dependence on electron temperature in the electron density region between $5 \times 10^{16}\,\mathrm{m}^{-3}$ and $5 \times 10^{18}\,\mathrm{m}^{-3}$.

As next step the model is benchmarked both versus ADAS (see paragraph 3.2) and experimental data.

Table 3.2: Left to right: The J quantum number of the higher excited state 13-$3p^4(^3P)4p(^4P)$, of the lower excited state 04-$3p^4(^3P)4s(^4P)$, the wavelength of the emitted photons, the Einstein coefficient for spontaneous emission and the statistical factor for the higher excited state of the transition [4].

Initial State J	Final State J	Wavelength (nm)	A_{ik}	ω_i
2.5	2.5	480.6	7.80×10^7	6
2.5	1.5	500.9	1.51×10^7	6
1.5	2.5	473.6	5.80×10^7	4
1.5	1.5	493.3	1.44×10^7	4
1.5	0.5	506.2	2.23×10^7	4
0.5	1.5	484.8	8.49×10^7	2
0.5	0.5	497.2	9.70×10^7	2

Table 3.3: Same quantities as in table 3.2. The higher excited state is 15-$3p^4(^3P)4p(^2D)$ and the lower excited state is 05-$3p^4(^3P)4s(^2P)$ [4].

Initial State J	Final State J	Wavelength (nm)	A_{ik}	ω_i
2.5	1.5	488.0	8.23×10^7	6
1.5	1.5	472.7	5.88×10^7	4
1.5	0.5	496.5	3.94×10^7	4

3.2 ADAS

The Atomic Data and Analysis Structure (ADAS) is an interconnected set of computer codes and data collections for modelling the radiation properties of ions and atoms in plasmas and for assisting in the analysis and interpretation of spectral measurements.

The three components of the package are an interactive system, a library of key subroutines, and a very large database of fundamental and derived atomic data. The interactive part provides immediate display of important fundamental and derived quantities used in analysis together with a substantial capability for preparation of derived data. It also allows exploration of parameter dependencies and diagnostic prediction of atomic population and plasma models. The second part is non-interactive but provides a set of subroutines which can be accessed from the user's own codes to draw in necessary data from the derived ADAS database. The database spans most types of data required for fusion and astrophysical application [10].

In this thesis work only one of the available interactive routines of ADAS was studied and used, therefore only this feature (i.e. the collisional radiative model) of a complex and multipurpose code is discussed.

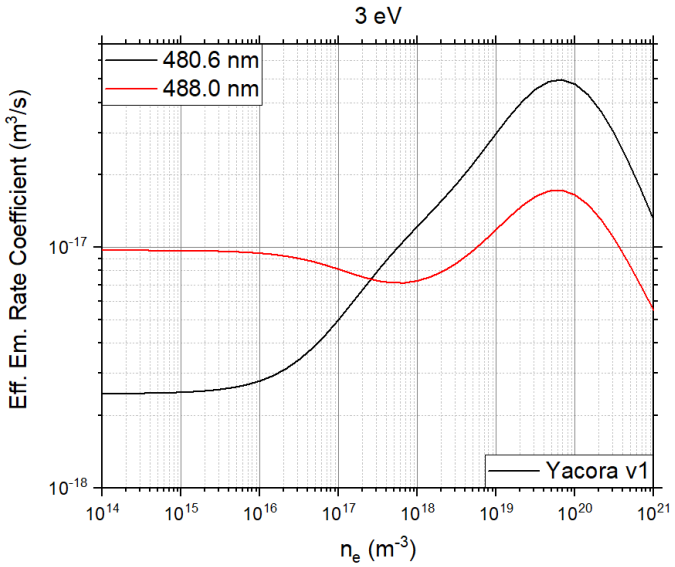

Figure 3.7: Effective emission rate coefficients for the 480.6 nm and 488.0 nm lines and an electron temperature of 3 eV

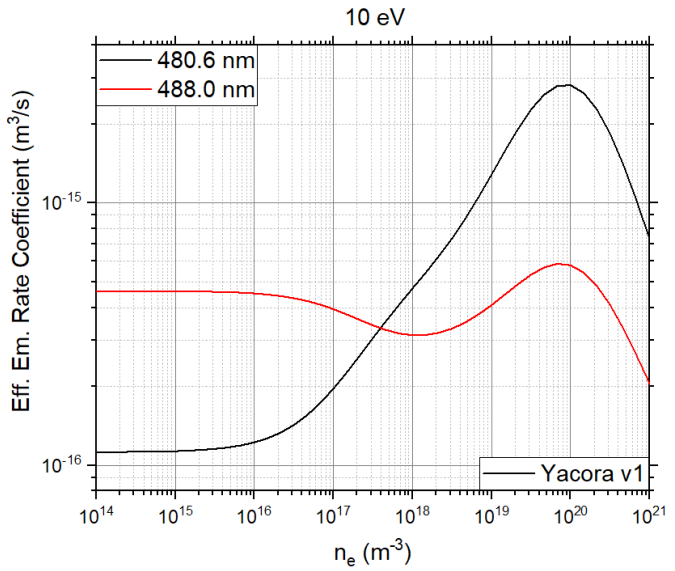

Figure 3.8: Effective emission rate coefficients for the 480.6 nm and 488.0 nm lines and an electron temperature of 10 eV

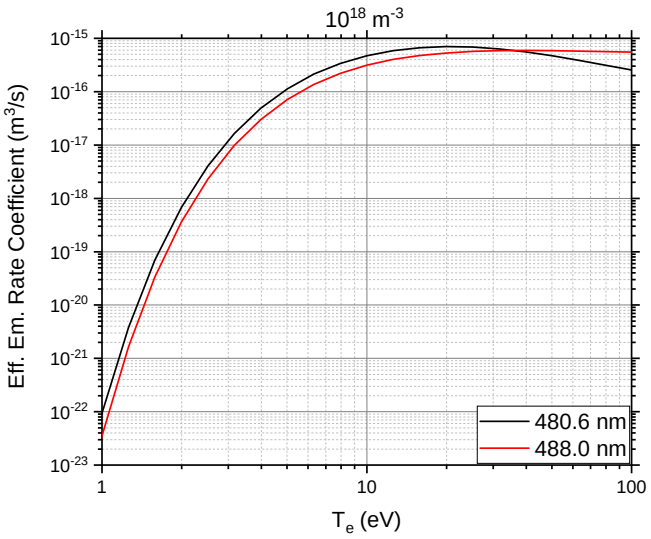

Figure 3.9: Effective emission rate coefficients for the 480.6 nm and 488.0 nm as a function of the electron temperature for an electron density of $1 \times 10^{18}\,\mathrm{m}^{-3}$.

3.2.1 ADAS810 Routine

ADAS810 is a subroutine of ADAS, which can solve the set of differential equations 1.29, as long as it is linear, for a wide variety of atoms.

As mentioned before, the purpose of the first version of the Yacora Ar^+ collisional radiative model is to reproduce the calculations of this subroutine. Thus the same input quantities, based on D. C. Griffin (2007) data [30], described in section 3.1 are provided to ADAS810: a list of energy levels, each one labelled with an index, average collision strengths (Υ_{ij}) for the electron collision excitation, as a function of electron temperature, and spontaneous emission Einstein coefficients for the optically allowed transitions.

This key subroutine allows the user to obtain effective emission rate coefficients between the states of the emitting particle species the user wants to simulate. Such effective emission rate coefficients are called "envelope feature photon emissivity coefficients" (PEC_{ij}) and, since the input file does not take into account fine structure splitting, describe spontaneous emission between Ar^+ non-resolved states.

PEC basically consists in the Einstein coefficient for non resolved state (A_{ij}) associated with the spontaneous emission between two chosen states multiplied by the equilibrium population coefficient of the upper state (R_i).

$$PEC_{ij} = R_i \cdot A_{ij} \tag{3.3}$$

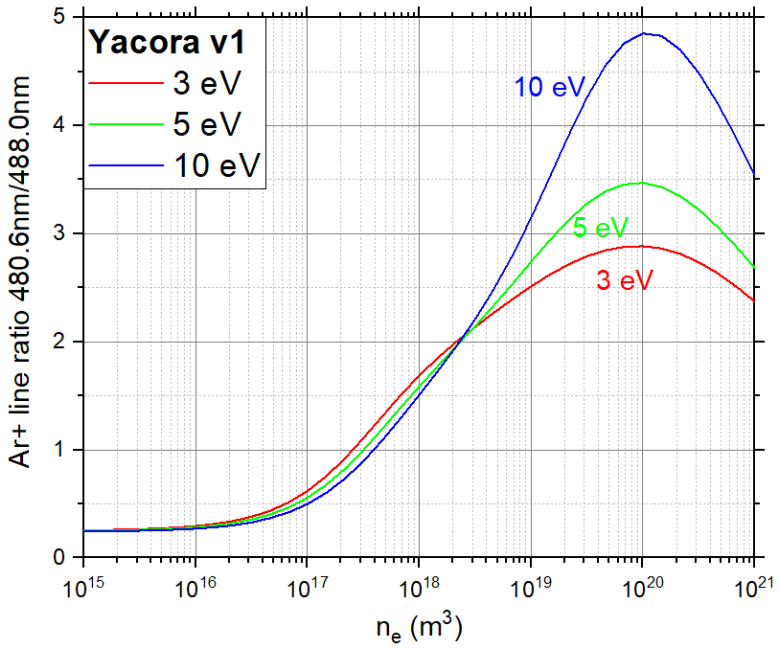

Figure 3.10: Ratio between lines 480.6 nm and 488.0 nm as a function of electron density for different electron temperature values.

since the 40 Ar^+ states defined in the input file based on D. C. Griffin (2007) are not fine structure resolved, the calculated PEC describes the sum of all transitions between a specific initial and final states, regardless of the J quantum number. The relation between Einstein coefficients for non resolved states (A_{ij}) and for single lines sharing the same upper and lower states ($A_{ij}(\lambda_k)$) is the following:

$$A_{ij} = \frac{\sum_l \omega_l A_{ij}(\lambda_l)}{\sum_l \omega_l} \tag{3.4}$$

in order to be consistent with the effective emission rate coefficient for a specific line ($X^{em}_{eff}(\lambda_k)$) defined with the equation 1.49, a branching ratio (br) has to be introduced. This quantity describes which fraction of that envelope is related to a particular transition. This works only if the population is statistically distributed.

$$br(\lambda_k) = \frac{\omega_k A_{ij}(\lambda_k)}{\sum_l \omega_l A_{ij}(\lambda_l)} \tag{3.5}$$

once this factor is evaluated, the effective emission rate coefficient for the specific line can be obtained.

$$X_{eff}^{em}(\lambda_k) = br(\lambda_k) \cdot PEC_{ij} = R_i \frac{\omega_k}{\sum_l \omega_l} A_{ij}(\lambda_k) \tag{3.6}$$

the statistical weight ω_k are defined in equation 1.20.

3.2.2 Yacora and ADAS Comparison

A very good agreement between the two codes is expected since both were used with input rate coefficients or average collisional strength based on the same set of reaction probabilities, published by D. C. Griffin in 2007, and both evaluate the same processes listed in section 3.1.2.

Figure 3.11 shows a comparison between the dependence of the effective emission rate coefficient for lines 480.6 nm and 488.0 nm on the electron density for two different electron temperatures. For determining the effective emission rate coefficients from the population coefficients, equation 1.49 was applied using the bold quantities listed in table 3.4. Equation 3.6 was applied to convert the PEC from ADAS into effective emission rate coefficients.

Table 3.4: Quantities used in calculations referred to lines 480.6 nm and 488.0 nm. Einstein coefficients and statistical factors were taken from NIST[4] while the branching ratio was evaluated according to equation 3.5.

Wavelength (nm)	$A_{ij}(\lambda)$ (s^{-1})	$\omega / \sum_k \omega_k$	branching ratio
$13 \rightarrow 4$	9.4×10^7		
473.6	5.8×10^7	0.33	0.206
480.6	7.80×10^7	**0.5**	**0.415**
484.8	8.49×10^7	0.17	0.151
493.3	1.44×10^7	0.33	0.051
497.2	9.70×10^6	0.17	0.017
500.9	1.51×10^7	0.5	0.080
506.2	2.23×10^7	0.33	0.079
$15 \rightarrow 5$	8.87×10^7		
472.7	5.88×10^7	0.4	0.265
488.0	3.23×10^7	**0.6**	**0.557**
496.5	3.94×10^7	0.4	0.178

It can be noticed, in figure 3.11, that the Yacora and ADAS predictions for the 488.0 nm effective emission rate coefficient do not match perfectly in the corona model region (i.e. $n_e < 10^{15}\,m^{-3}$) where, since only electron collision excitation from the ground state and spontaneous emission play an important role, the best accordance is expected. In contrast, the results of the two models for the 480.6 nm line are on top of each other.

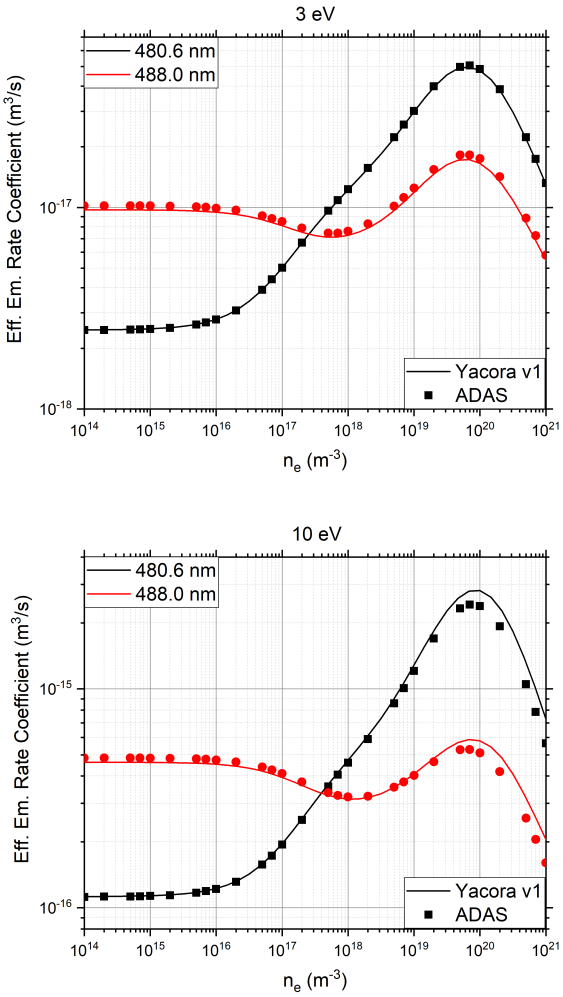

Figure 3.11: Comparison between effective emission rate coefficients from Yacora (previously shown in figures 3.7 and 3.8) and ADAS. Each graph represent a different electron temperature.

The slight mismatch for the 488.0 nm line at low n_e is caused by the fact that, as already mentioned, ADAS generates PECs which are obtained from the Einstein coefficients listed in Open-ADAS input files: these coefficients are referred to the transition probability between two states regardless of J quantum number. The value assumed in the D. C. Griffin (2007) database is $A_{ij}^{OA} = 9.31 \times 10^7\,\mathrm{s}^{-1}$. In the Yacora analysis, once the population coefficients have

been evaluated, Einstein coefficients for the specific emission line to be simulated are used. If, using equation 3.4, the NIST coefficients of each line between the same upper and lower excited levels are summed $A_{ij}^{NIST} = 8.87 \times 10^7\,\mathrm{s}^{-1}$ is obtained.

The same problem does not occur with line 480.6 nm because, in that case, the two databases contain Einstein coefficients that are in agreement with each other.

In order to prove that the mismatch was due to this difference, figure 3.12 shows the population coefficients of the upper states of the transitions at 480.6 nm and 488.0 nm, i.e. post processing the model results using different Einstein coefficients was suppressed.

A perfect match between the two predictions in corona model region can be seen. In the 10 eV case, for higher electron densities (approximately $> 10^{19}\,\mathrm{m}^{-3}$) there is still a difference by about 15% between the results of Yacora and ADAS. The reason for this is not entirely clear, but the differency in how Yacora and ADAS handle the input data might play a role. In order to reduce complexity, ADAS models can bundle several excited states (typically those with high energies) to one state. So, if such bundling is used for states that can spontaneously de-excite into state $15 - 3p^4(^3P)4p(^2D)$ (the upper state of the transition at 488.0 nm), the difference between the two predictions in the bottom graph of figure 3.12 could be explained since the densities of such excited states increase with both electron temperature and density.

Figure 3.13 shows the line ratio between the lines at 480.6 nm and 488.0 nm from ADAS and Yacora for a range of electron densities between $10^{15}\,\mathrm{m}^{-3}$ and $10^{21}\,\mathrm{m}^{-3}$. Again, slight differences can be noted that are due to the different used Einstein coefficients. If ADAS prediction is corrected by the ratio between the two different Einstein coefficients for 488.0 nm line: $\frac{9.31 \times 10^7\,\mathrm{s}^{-1}}{8.87 \times 10^7\,\mathrm{s}^{-1}} \simeq 1.05$, see figure 3.14, the agreement between the line ratio predictions from the two models improves also in the high electron density (approximately $> 10^{19}\,\mathrm{m}^{-3}$) region where emission effective rate coefficients show a slight mismatch.

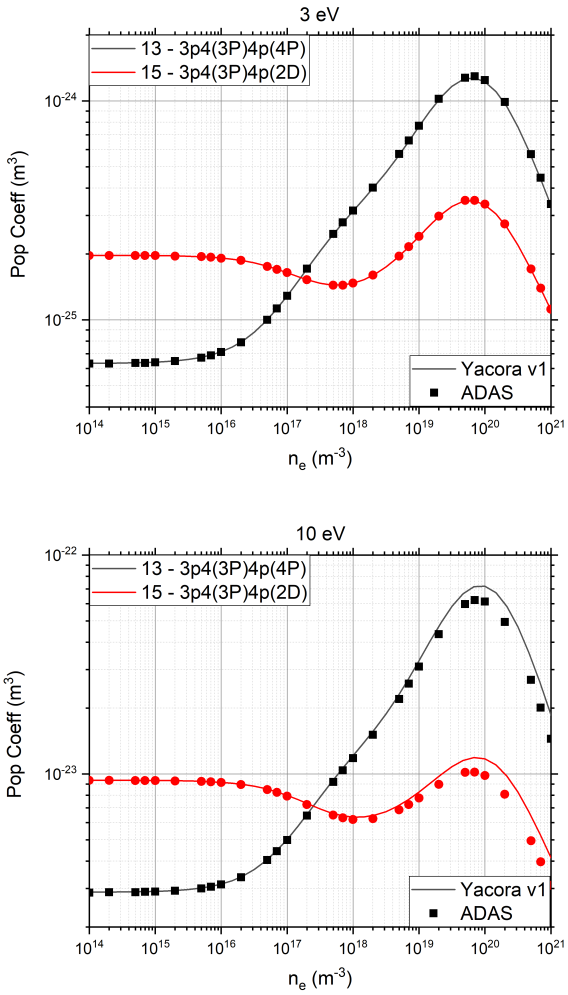

Figure 3.12: Comparison of population coefficients from Yacora and ADAS for the upper states of the emission lines 480.6 nm and 488.0 nm. The same conditions of figure 3.11 were used. The integer on the left hand side of the excited Ar^+ state name represent its index in D. C. Griffin (2007) database.

In conclusion, the benchmark with ADAS810 proved to be successful as the first version of the Yacora Ar^+ model manage to reproduce ADAS calculation within a 5 % factor.

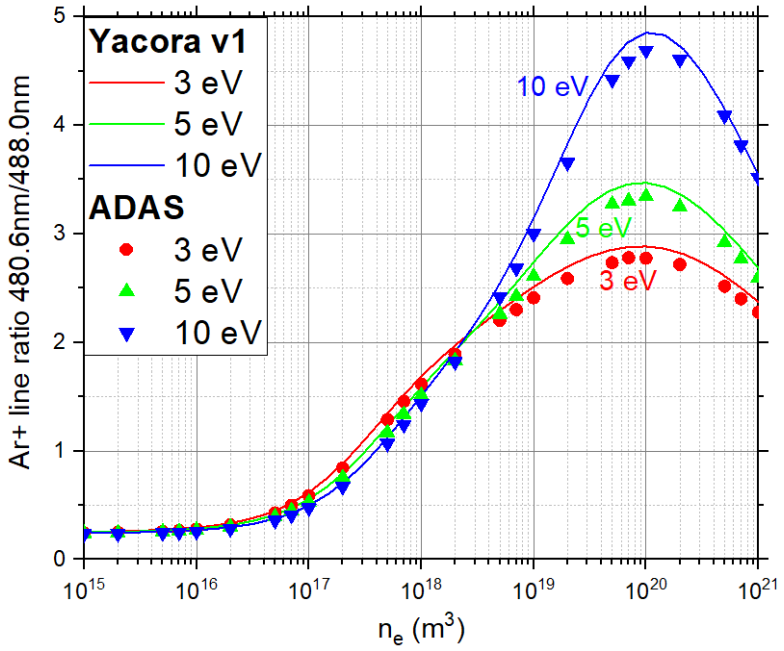

Figure 3.13: Comparison between Yacora and ADAS 480.6 nm and 488.0 nm line ratio prediction.

3.3 Beyond the Linear Model

Once the first version of the Yacora Ar^+ model has been successfully benchmarked versus ADAS, other potentially relevant processes can be implemented and the impact of these processes on the calculated population densities assessed.

3.3.1 Electron Collision Ionization

Collisions between electrons and Ar^+ ions can lead to a loss term in the population density of excited Ar^+ states due to the following process which can occur, for collision with an Ar^+ atom in the ground state, if the 27.63 eV energy threshold is exceeded [4].

$$e^- + Ar^+ \rightarrow 2e^- + Ar^{2+} \tag{3.7}$$

the used database for electron collision ionization is provided by A Müller [34]. It includes rate coefficients for electron collision ionization with three Ar^+ levels: $1 - 3s^2 3p^5(^2P)$ (the ground state), $3 - 3s^2 3p^4(^3P)3d(^4D)$, $6 - 3s^2 3p^4(^3P)3d(^4F)$. According to table 3.1, these states have the higher lifetimes

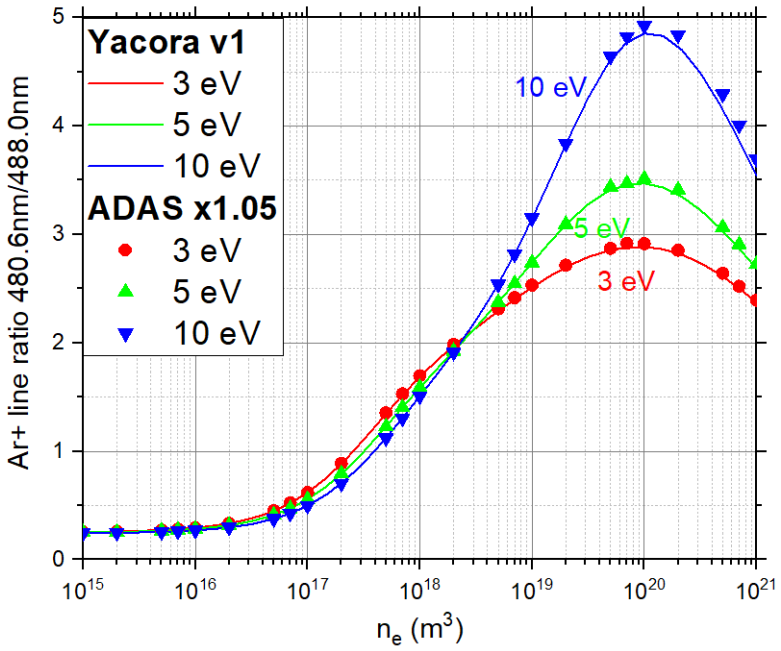

Figure 3.14: Same plot as in figure 3.13 but with ADAS prediction corrected by a factor determined by the ratio between the Einstein coefficient for line 488.0 nm from NIST and Open-ADAS databases.

and, according to Yacora simulations are usually the states with the highest densities together with the metastable state, for which, no data was available on Open-ADAS.

A fitting procedure as described in section 3.1.2 is not necessary since the number of available interpolation values of the rate coefficients for the ionizing transitions is 24.

The effect of adding ionization in the Yacora collisional radiative model for Ar^+ on effective emission rate coefficients is shown in figure 3.15. The ionization introduces an additional loss term into the set of coupled differential equations 1.29. Therefore, as expected, effective emission rate coefficients decreases as shown in figure 3.15.

Figure 3.16 shows the effect of electron collision ionization on the 480.6 nm to 488.0 nm line ratio. As expected, since such process is induced by collision with energetic electron, the effect is more evident for high electron densities (approximately $> 10^{18}\,\mathrm{m}^{-3}$) and higher electron temperatures (approximately $> 5\,\mathrm{eV}$). Such effect is explained by looking, for example, at the rate coefficient for electron collision ionization of the Ar^+ ground state, which is shown in figure 3.17 and compared with the electron collision excitation from the ground

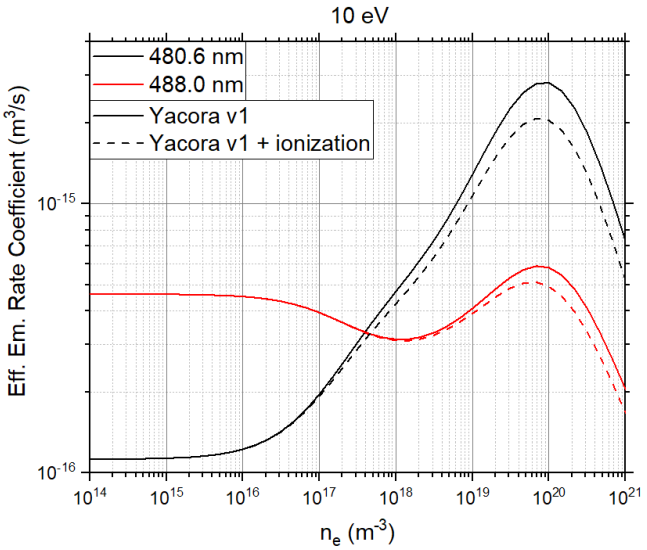

Figure 3.15: Yacora effective emission rate coefficient prediction at 10 eV for lines 480.6 nm and 488.0 nm.

state to the first excited state of Ar^+ $2-3p^5(^2P)$, which is the most important electron collision excitation process for Ar^+ ions at the ground state. For temperature above 8 eV second ionization becomes the most probable electron collision process with the ground state. This suggests that, for plasmas with electron temperature higher than 8 eV, ionization is important to include in the Ar^+ collisional radiative model. Also, cross sections for electron collision excitation for other excited states should be included when available as their overall effect might be relevant also at lower electron temperature.

3.3.2 Diffusion

Diffusion of excited states was added into a second version[1] of the Yacora model for Ar^+ as a loss term probability for each excited state density in a similar way used to treat spontaneous emission. A coefficient, which estimates a number of diffused and lost ions per second, is added into Yacora Ar^+ model based on the total confinement time defined in equation 1.39. As mentioned in section 3.1, diffusion can only be treated as a loss term and not as a transport term of species since Yacora provides zero dimensional models. Unlike spontaneous emission, the probability of losing ionized particles via diffusion depends on plasma parameters like pressure and temperatures. Such parameters, together with the mean free pathlength $\widetilde{\Lambda}$ and the mean diffusion length Λ for a cylindri-

[1] referred in the graphs as "Yacora v2", it includes the processes of the first version plus electron collision ionization and diffusion.

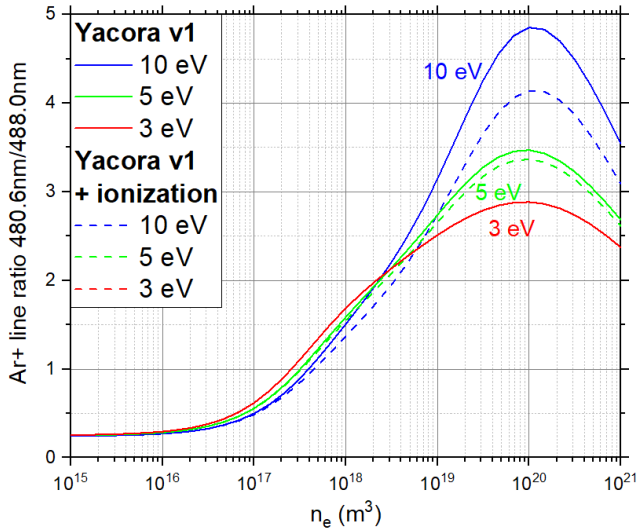

Figure 3.16: Yacora 480.6 nm and 488.0 nm line ratio prediction without (full line) and with ionization contribution (dashed line).

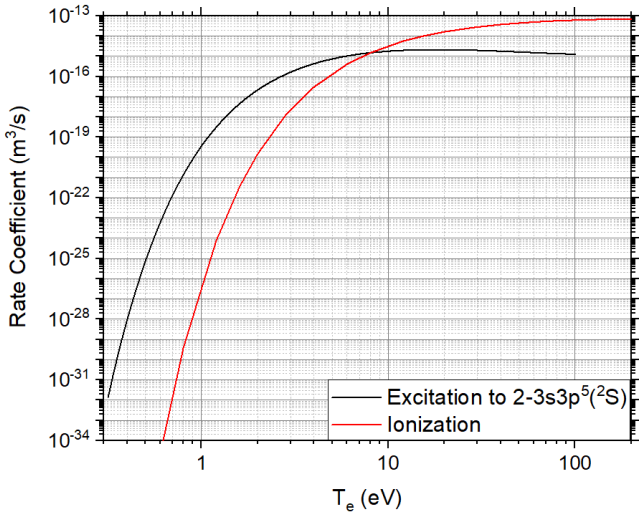

Figure 3.17: Comparison between rate coefficients as a function of the electron temperature from the Ar^+ ground state to the first excited Ar^+ state and to Ar^{++} respectively.

cal container defined in equations 1.42 and 1.44 respectively, were added into the Yacora Ar^+ model.

The reduced mobility μ_{red} for Ar^+ ion in an Ar background gas is tabulated as a function of an effective temperature (defined in equation 3.8) in an article published by H. W. Ellis et al. [35]. The choice of a background gas limits the application of the model since, if the predominant species of the plasma is not Ar, different values of the reduced mobility should be used according to the background of interest. An example of such situation is if Ar is added to other gas in small quantities as a diagnostic gas, as described in section 1.6.2.

$$\frac{3}{2}k_bT_{eff} = \frac{3}{2}k_bT_i + \frac{1}{2}Mv_d^2 \tag{3.8}$$

where M is the mass of the ion and $v_d = \mu_i E$ is the drift velocity, which is proportional to the electric field present in the plasma.

The values of the reduced mobilities are shown in figure 3.18. A fit, also shown in the graph, has been performed to approximate this quantity to a second order polynomial function (see equation 3.9) of the effective temperature logarithm.

$$\mu_{red} = a_0 + a_1 log(T_{eff}) + a_2 log^2(T_{eff}) \tag{3.9}$$

due to the plasma quasineutrality, the plasma potential profile can be assumed to be flat (in the absence of strong currents). Thus the effect of this electric field can be neglected outside the Debye sheath. Therefore the effective temperature (T_{eff}) can be approximated by the ion temperature (T_i).

Adding the loss of excited states due to diffusion required two diffusion lengths Λ and $\widetilde{\Lambda}$, the plasma pressure (p) and the effective temperature (T_{eff}) to be defined in the Yacora input text files.

Figure 3.19 shows the dependence of effective emission rate coefficients for the two transitions at 480.6 nm and 488.0 nm on the electron density plotted for several fixed values of the diffusion lengths Λ and $\widetilde{\Lambda}$. Figure 3.20 shows how the line ratio of these two lines is affected by diffusion.

It can be seen that for the line 488.0 nm also the electron density region in which the corona model is valid is strongly affected by diffusion.

The reason for this behaviour was understood due to the balance, which shows the contribution of all exciting and de-exciting reactions, provided by Yacora. It is due to the influence of the Ar^+ metastable excited level on one of its most probable products due to electron collision excitation: the excited state $19 - 3p^4(^1D)3d(^2F)$. Such Ar^+ excited state only decays, via spontaneous emission, into state $15 - 3p^4(^3P)4p(^2D)$ which is the upper state of the 488.0 nm transition. The balance output of Yacora which, as mentioned in section 3.1 provides for each excited state the contributions of all excitation and de-excitation reaction, shows that, for electron densities below $1 \times 10^{16}\,m^{-3}$, up to $\sim 30\,\%$ (depending on the input diffusion parameters) of the increase of state $19 - 3p^4(^1D)3d(^2F)$ population is due to electron collision with the metastable state. As mentioned before, metastable states do not decay via spontaneous emission so, in corona model region, the most important loss term is diffusion itself.

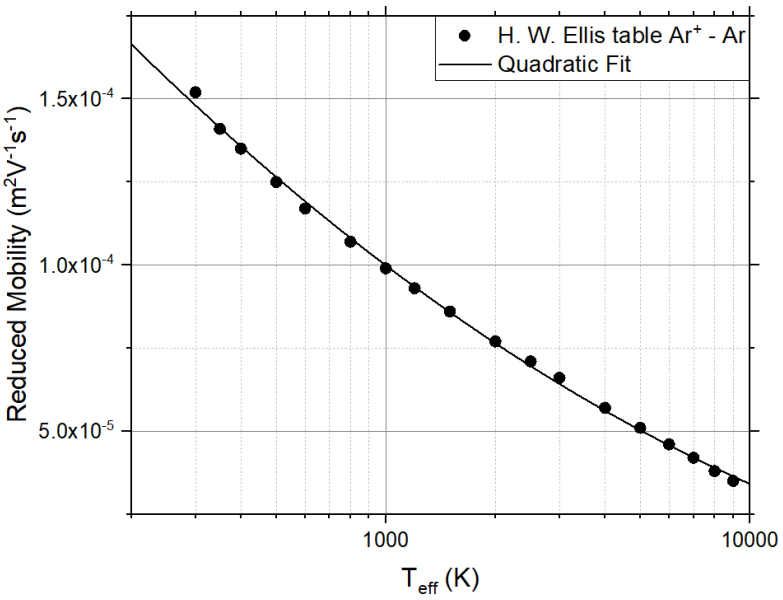

Figure 3.18: Reduced mobility, as function of an effective temperature, for Ar^+ ions in an Ar background [35].

Figure 3.21 shows the effect of diffusion on the metastable state population coefficient. Corona model region is heavily influenced by the choice of diffusion parameters; since that is the only relevant loss term, the black curve, which is the simulation where any diffusive process is neglected, does not show the constant behavior typical of corona model approximation region.

As for the 480.6 nm transition, all processes have a negligible influence on the population coefficient of its upper state.

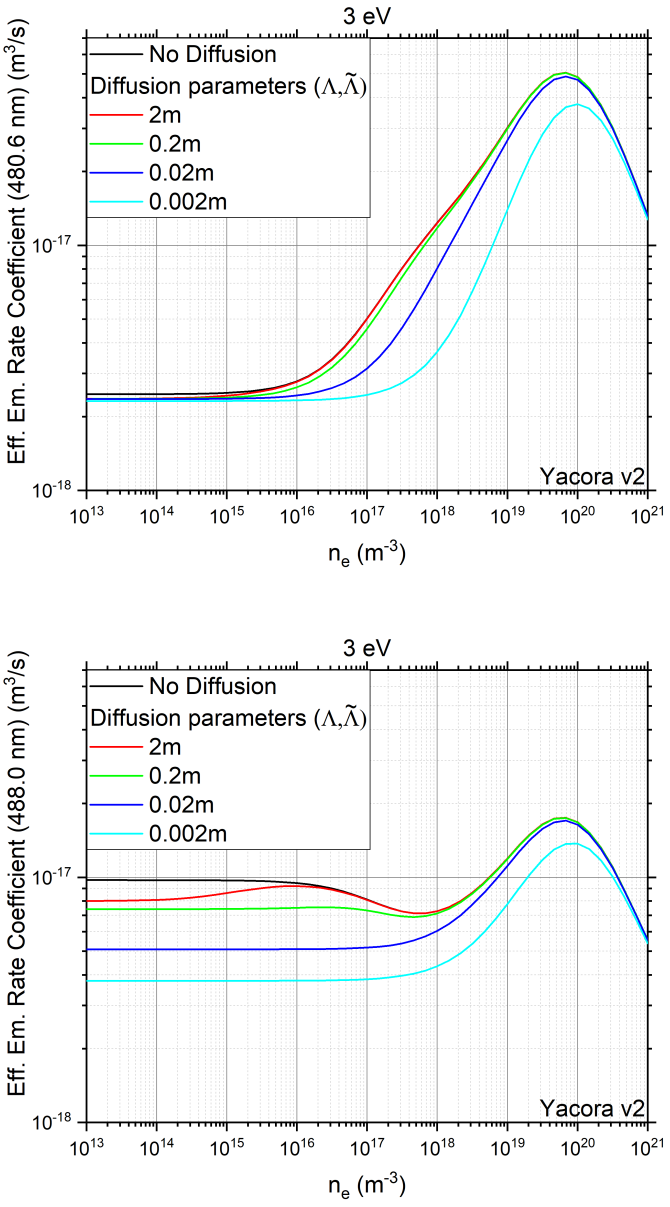

Figure 3.19: 480.6 nm and 488.0 nm effective emission rate coefficients for several diffusion coefficient values. $\Lambda = \widetilde{\Lambda}$ was set.

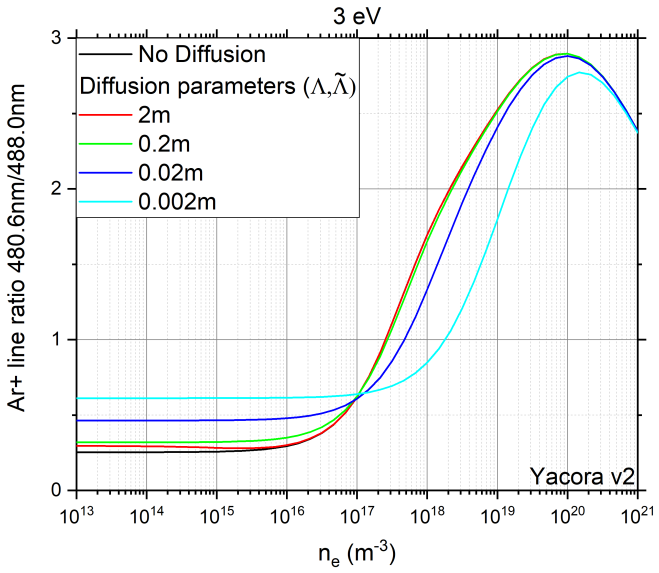

Figure 3.20: Line ratio of the lines plotted in figure 3.19 using the same conditions.

3.3.3 Heavy Particle Collisions

Two additional processes due to collisions between heavy particles were studied in order to include them into the Yacora Ar^+ model and increase its accuracy.

- Penning ionization
- Energy pooling

Penning reactions and energy pooling are relevant processes for argon plasmas. Their contribution as a loss term in the set of differential equations for a CR model (see equation 1.29) become increasingly important as the pressure approaches one atmosphere.

Penning ionization is a process in which an excited, usually in a metastable state, atom or molecule A^{**} collides with another atom or molecule B and transfers all its excitation energy into its target, ionizing it [36].

$$A^{**} + B \rightarrow A + B^+ + e^- \tag{3.10}$$

energy pooling refers to a vast class of phenomena related to energy transfer collisions, mainly between two atoms at their first excited level (A^*), where all the excitation energy is transferred to one of the colliding particle [37].

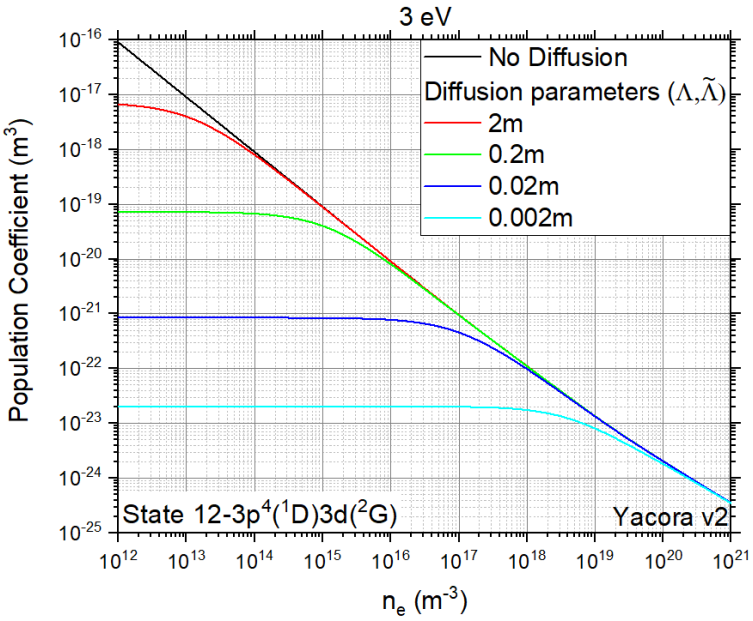

Figure 3.21: Population coefficient of the metastable Ar^+ level. $\Lambda = \widetilde{\Lambda}$ was set.

$$A^* + A^* \rightarrow A + A^{**} \tag{3.11}$$

however, no available rate coefficient for such processes in argon plasmas was found. Thus it was not possible to include them.

Chapter 4

Benchmark with the Experimental Data

In this chapter, experimental results both from PlanICE and from the HiPIMS experiment of Ruhr-University in Bochum are presented with different purposes. PlanICE is equipped with a movable Langmuir probe, so plasma parameters of the observed spectra are known a priori. For this reason, measurements performed at PlanICE are studied in order to benchmark the Yacora Ar^+ model by comparing its predictions with experimental measurements. For the HiPIMS experiment, only partial information on plasma parameters are available and spectra are only relatively calibrated. Therefore it can be considered as an example of how OES spectra analysis can provide a non invasive measurement on unknown plasma parameters.

4.1 PlanICE

Using the test facility described in section 2.1, Ar plasmas, in different conditions of gas pressure and RF power, were generated. These conditions are summarized in table 4.1 and plotted in figure 4.1. In addition, electron densities n_e and temperatures T_e, measured with the movable Langmuir probe, are also provided. Errors on n_e and T_e from Langmuir probe measurements are assumed to be around 50 % and $20 - 25$ %, respectively [38].

The relation between the number of emitted photons defined in equation 1.28 and the quantities used by Yacora is the following.

$$N_{ph} = n_p \frac{\omega_k}{\sum_l \omega_l} A_{ij}(\lambda_k) = n_0 n_e R_{0p} \frac{\omega_k}{\sum_l \omega_l} A_{ij}(\lambda_k) \tag{4.1}$$

where ω_k is the statistical factor of the upper state associated with the transition line λ_k. Using equation 1.49, the number of photons can be related to effective emission rate coefficients ($X^{em}_{eff}(\lambda_k)$)

Table 4.1: List of parameters of the generated Ar plasmas on PlanICE [38].

Pressure (Pa)	RF Power (W)	n_e (m^{-3})	T_e (eV)
0.3	300	1.7×10^{17}	6.7
1	300	2.5×10^{17}	4.7
1	400	3.4×10^{17}	4.7
1	500	4.5×10^{17}	4.5
3	300	7.5×10^{17}	2.7
4	300	1.0×10^{18}	2.5
5	300	1.2×10^{18}	2.3
6	300	1.4×10^{18}	2.3
7	300	1.7×10^{18}	2.2
8	300	1.9×10^{18}	2.1
9	300	2.1×10^{18}	2.0
10	300	2.2×10^{18}	2.0

$$N_{ph} = n_0 n_e X^{em}_{eff}(\lambda_k) \tag{4.2}$$

according to the discussion in section 3.1.3 referring to figure 3.5, where it is shown that for Ar^+ the ground state population coefficient is much higher than those of the excited states, $n_p \ll n_0$ is assumed. Thus, since Ar is the only species in the observed plasma, such approximation, together with the quasi-neutrality condition of a plasma, provides the condition $n_0 = n_{Ar^+} = n_e$.

The error on the number on the effective emission rate coefficient $X^{em}_{eff}(\lambda_i)$ determined using OES is usually around 5 % [38]. Since it is much smaller than the relative error on the plasma parameters evaluated with the Langmuir probe, the error due to the spectrometer is not shown in the figures of this section.

Errors on the effective emission rate coefficients imply that the error σ_R associated with a line ratio measurement R_{λ_k/λ_l}, defined with equation 1.51, is:

$$\sigma_R^2 = \left(\frac{\sigma(\lambda_k)}{X^{em}_{eff}(\lambda_l)}\right)^2 + \left(\frac{X^{em}_{eff}(\lambda_k)}{(X^{em}_{eff}(\lambda_l))^2}\sigma(\lambda_l)\right)^2 \tag{4.3}$$

where $\sigma(\lambda_i)$ is the error associated to the effective emission rate coefficient $X^{em}_{eff}(\lambda_i)$.

In this chapter, each measured line ratio value is between 0.5 and 2. Thus, by assuming $X^{em}_{eff}(\lambda_k) = X^{em}_{eff}(\lambda_l)$ in equation 4.3, $\sigma_R \simeq 7\,\%$ is assumed.

4.1.1 Fine Structure Splitting

In order to test the reliability of the assumptions made in section 3.1.3 about fine structure splitting calculations, the effective emission rate coefficients for each transition between the non resolved Ar^+ states $13-3p^4(^3P)4p(^4P)$ and $4-$

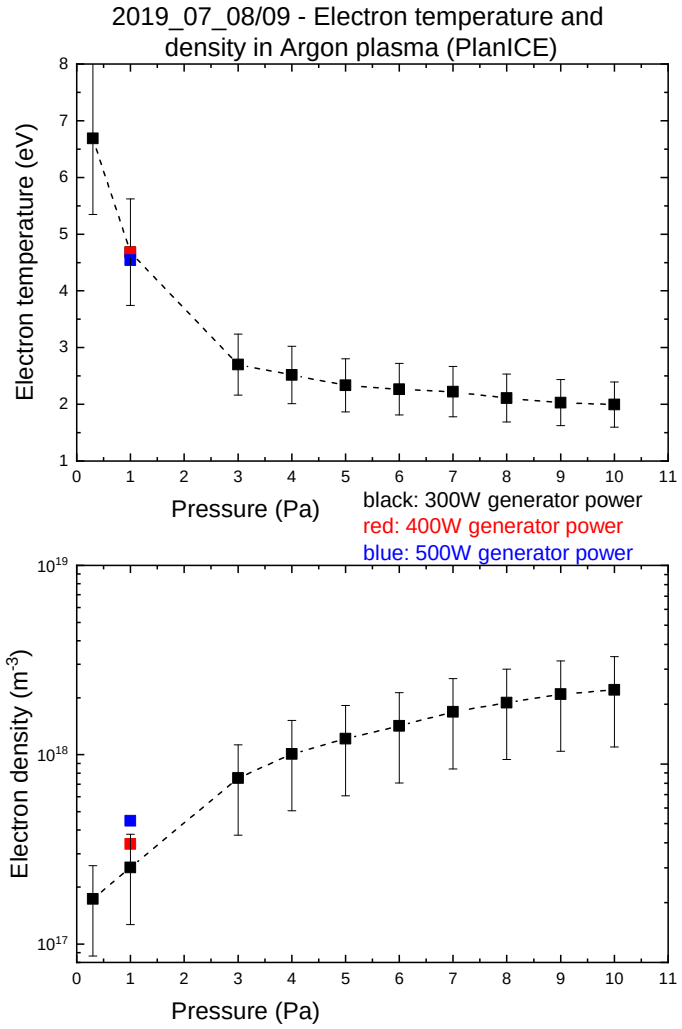

Figure 4.1: Electron temperature and density as a function of the pressure. The plotted points are listed in table 4.1.

$3p^4(^3P)4s(^4P)$ was measured. These transitions are chosen for the comparison since three different quantum number J values can be assumed for the upper state $13 - 3p^4(^3P)4p(^4P)$ and each transition is visible in the acquired spectra. Among them, the line at 480.6 nm is the most probable transition.

On the left hand side of figures 4.2 and 4.3, the branching ratios (defined with equation 3.5) associated to each transition between the two mentioned states from Yacora and determined from the OES measurement is plotted. Values

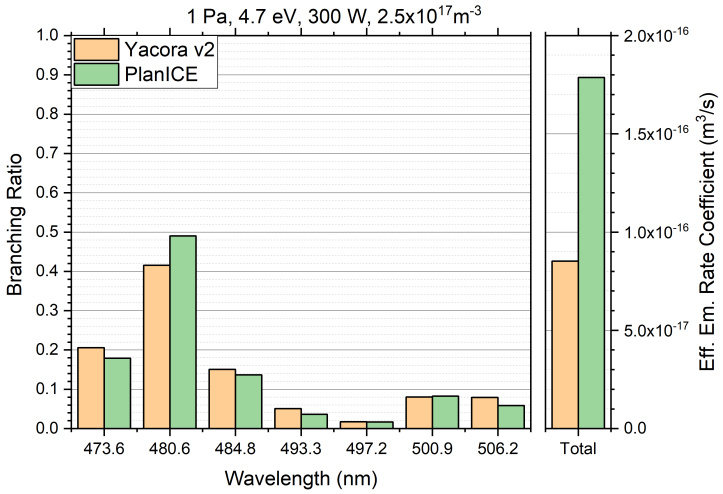

Figure 4.2: Left: Comparison between the expected branching ratios values used on Yacora, and those obtained from PlanICE measurements. Ar gas pressure was set to 1 Pa and the RF power to 300 W. Right: The sum of the effective emission rate coefficients measured at PlanICE for each of the considered lines compared with the prediction by Yacora.

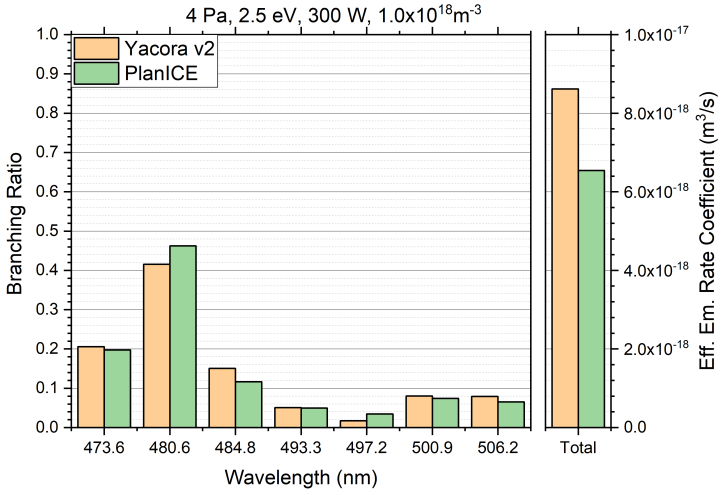

Figure 4.3: Same plot as figure 4.2. Ar gas pressure was set to 4 Pa and the RF power to 300 W.

used in Yacora output file analysis are shown. These are obtained using data available on NIST according to equation 3.5. With them, the ratios between the number of photons measured by OES associated to each transition and the sum of the measured photons, evaluated with equation 4.2 in the seven transitions are shown. Assuming a statistical distribution this ratio does not depend on plasma parameters. Thus any difference between the branching ratio, measured in PlanICE, relative to the same line in the two graph can be assumed to be due to uncertainties of the optical spectroscope.

The result confirms the branching ratios evaluated and used for Yacora output population coefficient analysis since both figures 4.2 and 4.3 show an agreement with the expected branching ratio.

On the right hand side of figures 4.2 and 4.3, the effective emission rate coefficients for each of the seven considered lines are summed. The plots show both the prediction by the Yacora Ar^+ model and the measurements in PlanICE. Since, as mentioned before, it is the sum of each transition from state $13 - 3p^4(^3P)4p(^4P)$ to state $4 - 3p^4(^3P)4s(^4P)$ such value does not depend on the branching ratio. Yacora Ar^+ model prediction and PlanICE measured effective emission rate coefficients do not match by a factor ~ 2. This might in principle be due both to inaccuracies by the Yacora Ar^+ model and to uncertainties in the plasma parameters measured with the movable Langmuir probe which are not taken into account in the right hand side of figures 4.2 and 4.3. Such differencies are discussed more in detail in section 4.3.

A similar behaviour was observed also for the comparison based on the transitions between the excited states $15-3p^4(^3P)4p(^2D)$ and $5-3p^4(^3P)4s(^2P)$ (which lines are listed in table 3.4). Thus the figures relative to such transition are not shown.

4.2 Diffusion

As mentioned in section 2.1, the PlanICE plasma chamber is a cylinder with 15 cm diameter and 10 cm height. Using equations 1.42 and 1.44 it is possible to evaluate the diffusion parameters associated with the experiment, which are:

$$\begin{cases} \widetilde{\Lambda} = 0.1\,\mathrm{m} \\ \Lambda = 0.02\,\mathrm{m} \end{cases} \tag{4.4}$$

as already mentioned in section 1.3 and shown in figure 3.21, the population coefficient of a metastable state strongly depends, especially at lower electron densities, on diffusion since it is the main loss term. Thus, in order to benchmark the effects of diffusion evaluated by the Yacora Ar^+ model, its predictions have to be compared with PlanICE measurements on the effective rate coefficients of a transition from an upper excited state which is heavily influenced by the metastable state $12 - 3p4(^1D)3d(^2G)$. In order to identify such excited state, the excitation rate coefficients for the electron collisions with the metastable

state, was checked in the database used as input for the Yacora Ar^+ model [30]. The most likely final state of such process, according to that database, is the excited state $21 - 3p^4(^1D)4p(^2F)$. For such excited state, the balance output of Yacora predicts that, for plasma condition similar to what is measured in PlanICE ($n_e = 1 \times 10^{18}\,\mathrm{m}^3$ and $T_e = 3\,\mathrm{eV}$), $\sim 25\,\%$ of the electron collision processes with the excited state $21 - 3p^4(^1D)4p(^2F)$ as the final state have the metastable as the initial state. Thus, it is expected that the effective emission rate coefficient of a spontaneous emission transition from such excited state is heavily influenced by diffusion.

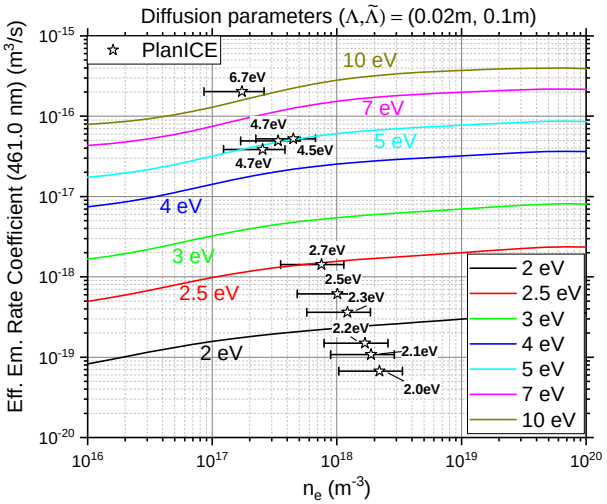

Figure 4.4: Comparison between effective emission rate coefficients for the line 461.0 nm measured at PlanICE and Yacora simulations. The diffusion parameters used for Yacora predictions are set according to the expected values (see equation 4.4) The electron densities and temperatures associated to each point were determined using a Langmuir probe.

As shown in figures 4.4 and 4.5, the 461.0 nm transition was measured at PlanICE against the electron density. Such wavelength corresponds to the transition with the highest Einstein coefficient from state $21 - 3p^4(^1D)4p(^2F)$ with and has $9 - 3p4(^1D)4s(^2D)$ as the final state. Each measured point is labelled with the corresponding electron temperature. It should be reminded that an error on electron temperature of about $20 - 25\,\%$ should be assumed.

The full lines show the Yacora Ar^+ model predictions. The choice on the pressures imposed in the simulations is based on PlanICE parameters listed in table 4.1 and shown in figure 4.1. The diffusion parameters written above each graphs represent the value used as input in Yacora simulations. The bigger graph on the bottom is the simulation with the diffusion parameters evaluated

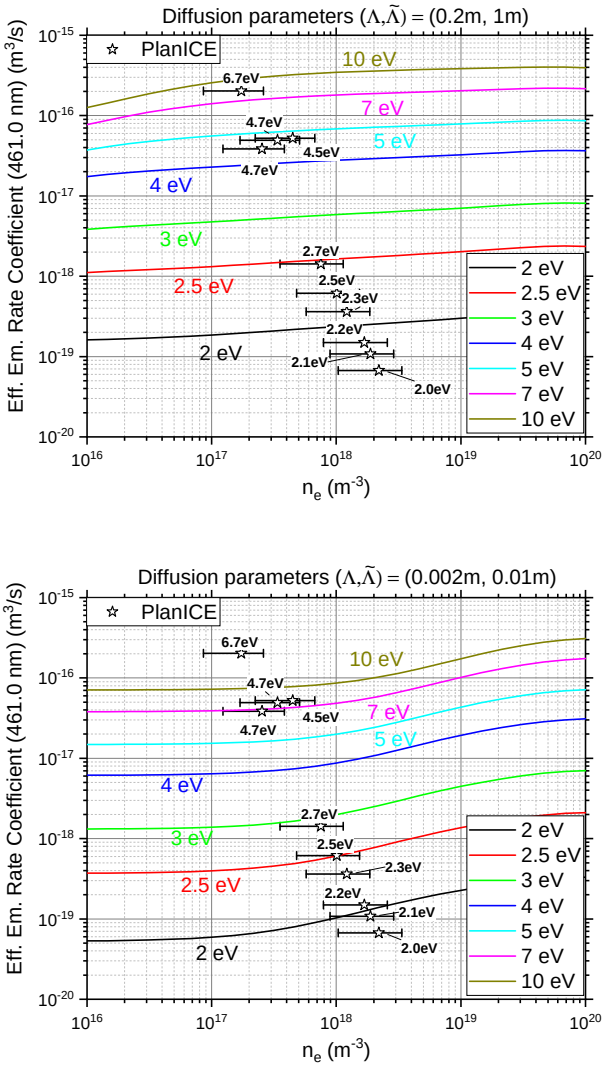

Figure 4.5: Same as figure 4.4 but with different sets of diffusion parameters used in each graph. Bottom: parameters an order of magnitude higher than expected are used. Top: parameters an order of magnitude lower than expected are used.

for PlanICE.

As expected, by increasing the mean diffusion length Λ and the average connection length $\tilde{\Lambda}$ (top-left hand side graph) particle loss due to diffusion be-

comes less important. For electron densities $n_e > 1 \times 10^{18}\,\mathrm{m}^3$, electron collision de-excitation dominates as a loss term and no difference can be seen with the simulation using the parameters expected from PlanICE. In each of the plots shown the effective emission rate coefficient evaluated by Yacora underestimate thePlanICE measurement at 6.7 eV. The Yacora Ar^+ model with the set with the lowest diffusion parameters is clearly underestimating higher temperature ($T_e > 4\,\mathrm{eV}$) effective rate coefficients. Both the set with the parameters evaluated for PlanICE (see equation 4.4) and the set where diffusion parameters are higher gives similar results which are in agreement with the experimental data. The large errors on Langmuir probe measurements, both on the electron density and on the electron temperature do not allow to state which of the two sets of parameters better describe the measurements. In conclusion, diffusion seems to be correctly implemented. However, spectra from plasmas with lower electron densities might help due to a higher sensitivity on diffusion.

4.3 General Behaviour

The comparison between effective emission rate coefficients measured at PlanICE and evaluated by Yacora for lines 480.6 nm and 488.0 nm are shown in figure 4.6.

The trend shown is similar to figure 4.4: taking into account the uncertainties on the electron temperatures T_e from the Langmuir probe, Yacora Ar^+ model predictions suit very well experimental effective emission rate coefficients below 3 eV. Rates at higher temperatures are underestimated by Yacora. This is more evident on the bottom graph of figure 4.6 showing the effective emission rate coefficients of line 488.0 nm, where, in the electron density range in which PlanICE operates, curves are constant with respect to the electron density.

The lines 480.6 nm and 488.0 nm ratios experimentally measured at PlanICE and predicted by Yacora are shown in figure 4.7. Due to its monotonically increasing dependency on electron density in the range swept by PlanICE ($1 \times 10^{17}\,\mathrm{m}^{-3} < n_e < 5 \times 10^{18}\,\mathrm{m}^{-3}$), this line ratio can be used to estimate the electron density. The procedure for obtaining the electron density from OES measurements is the following.

The electron temperature of the observed Ar plasma was measured using the movable Langmuir probe. For each experimental line 480.6 nm and 488.0 nm ratio measured at PlanICE, the curve, simulated by Yacora at the same electron temperature, is considered. The line ratio method prediction on electron density is the electron density value that corresponds to the experimentally determined line ratio. An example of such procedure is shown in figure 4.8. These electron densities are plotted in figure 4.9 as red dots. The error bars associated to electron density predictions by Yacora are evaluated by repeating the same procedure with curves at electron temperatures higher and lower than the measured one by $20 - 25\,\%$. When repeating such procedure the error bars associated with the line ratio are taken into account as shown in figure 4.8. In

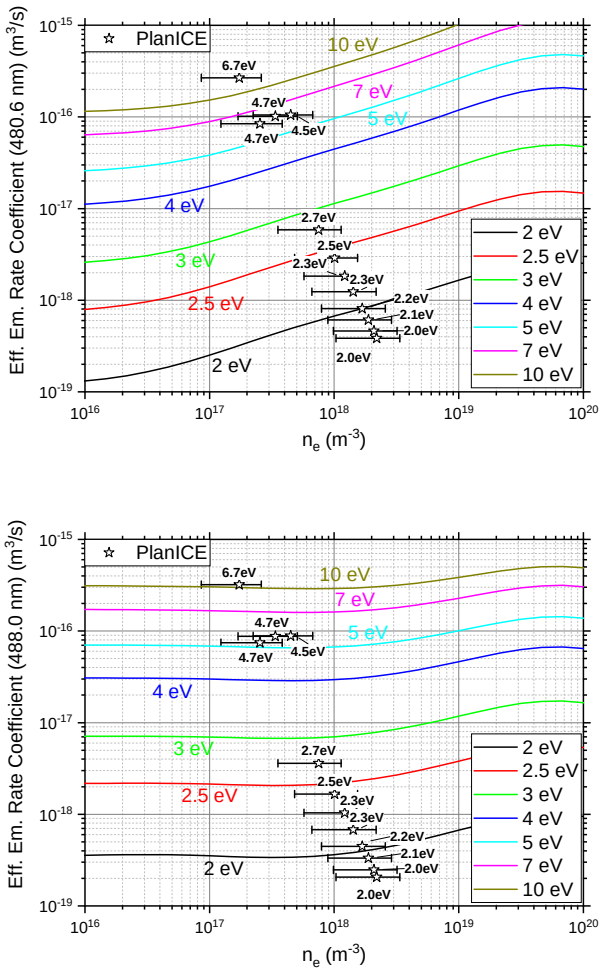

Figure 4.6: 480.6 nm and 488.0 nm effective emission rate coefficients predicted by Yacora for several electron temperatures (curves) and measured with OES spectroscopy on PlanICE Ar plasma in the conditions listed in table 4.1 (stars).

the same graph, black dots are the electron densities measured with the Langmuir probe. The graph only shows measurements with RF power imposed to 300 W.

The comparison between the two methods shows that, taking errors into accounts, OES electron density measurements are compatible with Langmuir probe ones. The two points at lowest pressures, which according to table 4.1 and figure 4.1 have the two highest measured electron temperatures (6.7 eV

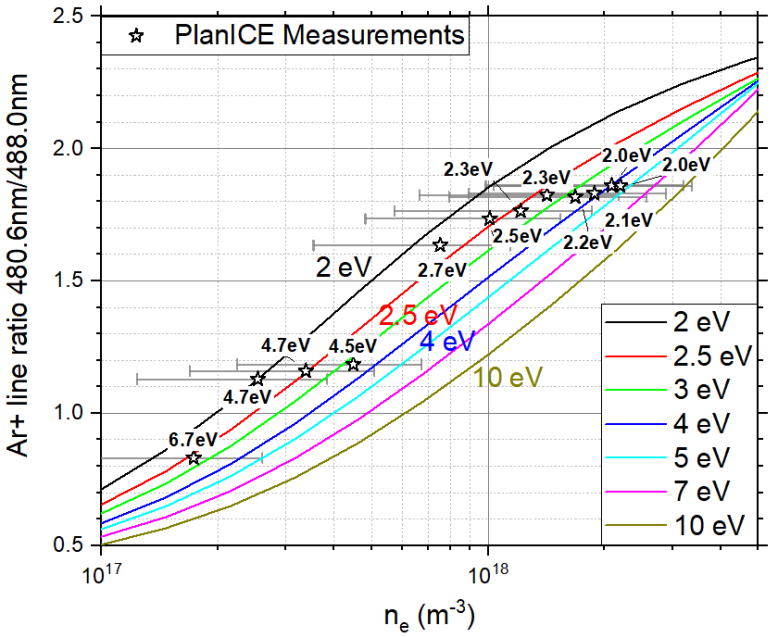

Figure 4.7: Line ratio of the lines plotted in figures 4.7. Curves and stars represent Yacora predictions and ratios measured from OES spectra respectively. The electron densities and temperatures associated to each point were determined using a Langmuir probe. The errors on the line ratio are of $\simeq 7\,\%$.

and 4.7 eV), are the only ones which show no overlap between the electron density predictions with the two methods. This is due to the small error bars, caused by Yacora line ratio curves to be more and more narrow as the electron temperature increases. But also reflects the mismatch shown in the effective emission rate coefficients in figures 4.6, where the electron temperature of the two mentioned points is overestimated. However, the shape of the electron densities estimation of Yacora is different form the one of the Langmuir probe measurements. This indicates that some processes might be missing. Additional benchmarks with plasmas at higher pressures may show if the difference in shape persists or if the prediction by Yacora are still compatible with the Langmuir probe measurements

Electron temperature can also be evaluated from the Yacora Ar^+ model. As shown on the bottom graph of figure 4.6, using the diffusion parameters evaluated for PlanICE, the effective emission rate coefficient for line 488.0 nm does not depend on electron density. This was exploited in order to evaluate the electron temperatures from the OES measurements. Figure 4.10 shows the effective emission rate coefficient as a function of the electron temperature both from Yacora simulations and from the OES measurements. As previously done

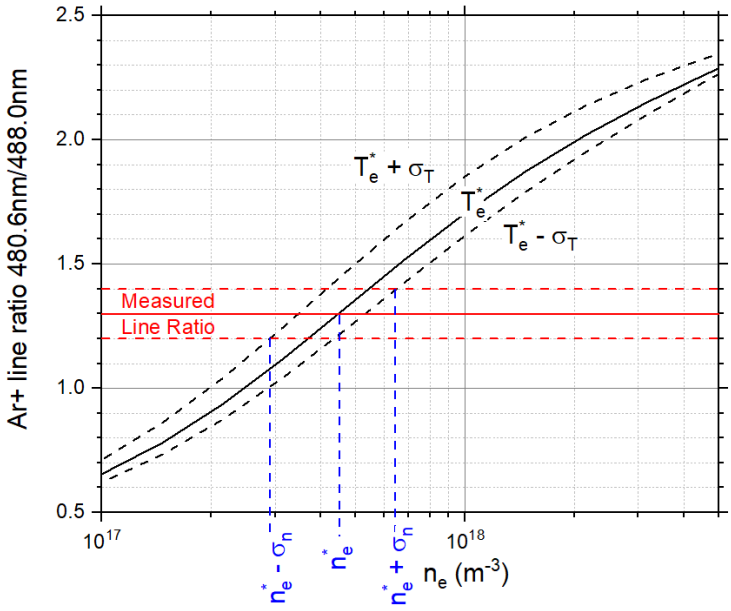

Figure 4.8: Example of how the errors on the electron densities are determined.

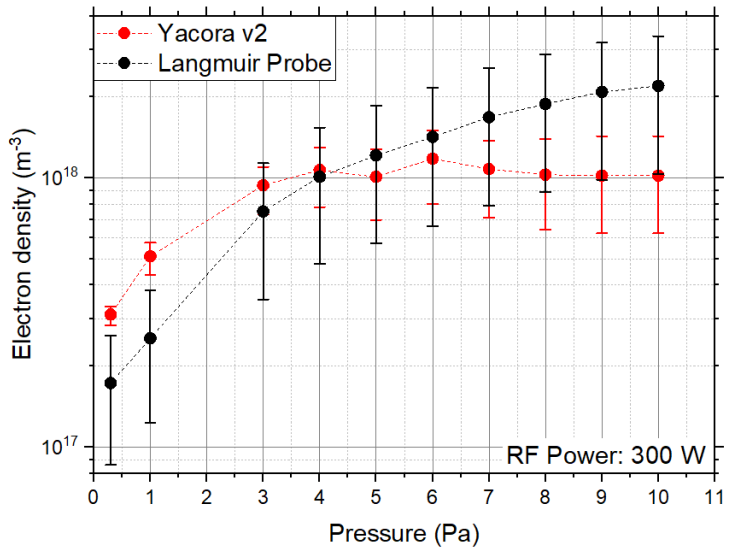

Figure 4.9: Comparison between the electron densities measured with the Langmuir probe (black) and the Yacora Ar^+ model predictions based on OES (red).

for figure 4.9, given an experimental effective emission rate coefficient, the corresponding electron temperature was extrapolated from the Yacora Ar^+ model prediction. Due to the independency of such effective emission rate coefficient from the electron density, the error associated to the electron temperature cannot be evaluated as shown in figure 4.8.

The electron temperatures evaluated from Yacora predictions are compared with the values provided by the Langmuir probe in figure 4.11. There is a good agreement at higher pressures ($> 2\,\mathrm{Pa}$) where both methods show a good compatibility. However, similarly to what is shown in figure 4.9, at $0.3\,\mathrm{Pa}$ there is a difference of a factor of 2 between Yacora estimation and the Langmuir probe prediction and a difference in shape can be noticed as well both in figures 4.10 and 4.11.

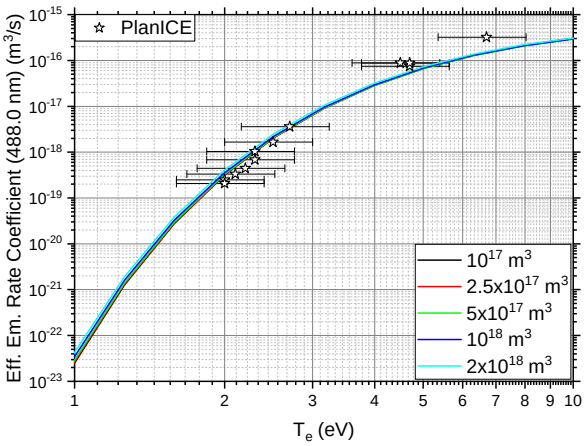

Figure 4.10: 488.0 nm effective emission rate coefficient measured at PlanICE (stars) in comparison with Yacora predictions (lines). Several lines for different electron densities are plotted.

In principle, this analysis can be performed also for VUV lines which, as mentioned in section 1.6, are of high relevance in surface processing plasmas. However, two problems arise in doing so. An absolute calibration is much more difficult to perform: the available Ulbricht sphere is not applicable in the VUV range. This makes the line ratio method the only possible analysis for plasma parameter determination. However, only two Ar^+ lines are intense enough to be distinguished in most of the spectra measured at PlanICE: lines 92.0 nm and 93.2 nm. These are the two resonance transitions from the first excited Ar^+ state $2-3s3p^6(^2S)$ to the ground state $1-3p^5(^2P)$.

Therefore, according to equation 1.49, the effective emission rate coefficient $X^{em}_{eff}(\lambda_k)$ for both lines depends on the population coefficient of state

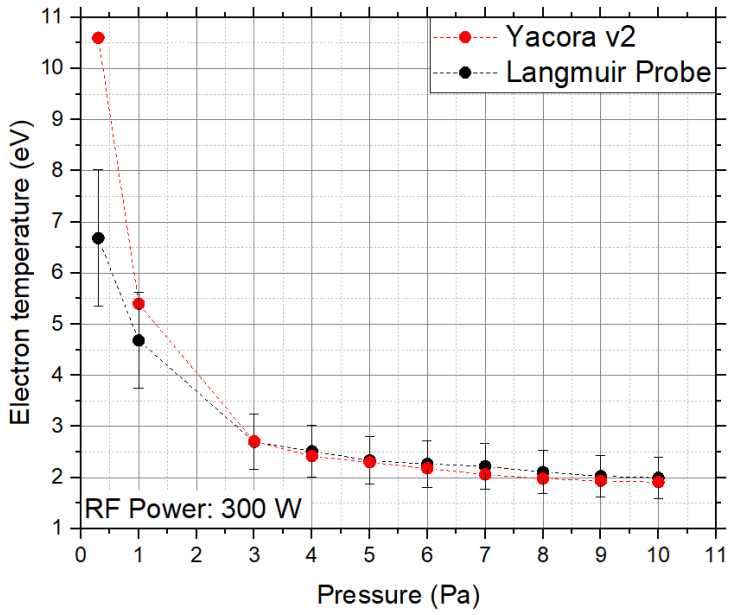

Figure 4.11: Comparison between the electron temperatures measured with the Langmuir probe (black) and the Yacora Ar^+ model predictions based on OES (red).

$2-3s3p^6(^2S)$. This means that the ratio between these two lines only depends on the statistical factors and on the Einstein coefficients related to the two transitions. Since such quantities do not depend on plasma parameters, a ratio between them would contain no information on plasma parameters.

In conclusion, the benchmark showed that, as for the ranges of the plasma parameters covered with PlanICE, Yacora Ar^+ model provides results which are compatible with the OES measurements. However, the differences in the shapes of both the electron density and temperature as a function of the pressure suggest that some processes might be missing and that additional benchmarks for higher electron densities and temperatures are required.

4.4 HiPIMS

As described in section 1.6.1, the plasma generated in an HiPIMS experiment allows to check the model at electron densities around $1 \times 10^{19}\,\mathrm{m}^{-3}$. Thus, the analysis of the spectra measured in the HiPIMS experiment in operation at the Institute for experimental physics II of Ruhr-University in Bochum was performed with the purpose of having an additional benchmark for different conditions with respect to those available for the PlanICE experiment. The analyzed spectra, together with a description of the operating conditions, were provided by E. Iglesias[1].

The HiPIMS experiment was operated with an Ar plasma and an Al sputtering target. The gas pressure in the chamber was fixed at 0.5 Pa. A variation of peak discharge current between 10 A and 50 A was provided [26]. An increase of such current implies the generation of an Ar plasma with a higher density of free electrons.

However, no information on the electron density in the region close to the target, which as mentioned in section 1.6.1 has the highest density, is available since no Langmuir probe was operating. As a reference electron density, the value of $6 \times 10^{19}\,\mathrm{m}^{-3}$ is assumed based on a literature measurement [39][26].

The electron temperature is expected to be between 2 eV and 5 eV [25], therefore these two temperatures are used as extreme values for the following simulations. Spectra were acquired using the Echelle spectrometer which, as mentioned in section 2.2, has a resolution of about $\Delta\lambda \simeq 30\,\mathrm{pm}$. An example of one of the analyzed spectra in the region of the two mentiond Ar^+ lines is shown in figure 4.12.

For each of the available spectra, The intensity of the Ar^+ lines at 480.6 nm and 488.0 nm were evaluated. As mentioned before, an absolute calibration of the used spectroscopic system is not available, therefore the analysis with effective emission rate coefficients cannot be performed and the line ratio method has to be used.

Table 4.2 summarizes the line measured ratio between the lines at 480.6 nm and 488.0 nm.

Table 4.2: Lines 480.6 nm and 488.0 nm ratios measured for each spectrum. An error of 5 % should be assumed.

Discharge Current (A)	Lines 480.6 nm/488.0 nm Ratio
10	0.91
20	1.31
30	1.29
40	1.41
54	1.30

[1] "Allgemeine Elektrotechnik und Plasmatechnik" (AEPT), Ruhr-University Bochum, Universitätstr 150, 44801, Bochum, Germany.

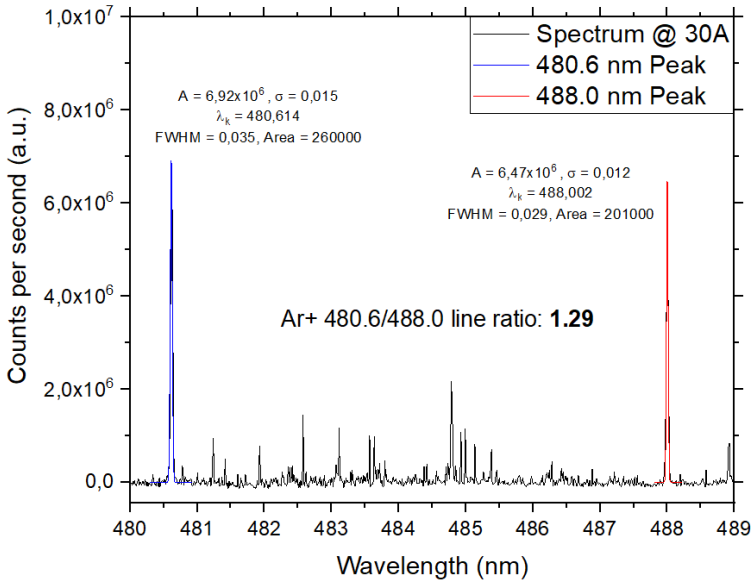

Figure 4.12: Section of the HiPIMS spectrum for an Ar-Al plasma for a discharge current of 30 A with the lines of interest indicated. Courtesy of E. Iglesias [26].

In order to simulate the ratio of the lines at 480.6 nm and 488.0 nm with Yacora and be able to determine a prediction for the electron density, the correct diffusion parameters has to be evaluated. As mentioned in section 2.2, the HiPIMS experiment under investigation has a cylindrical plasma chamber with 40 cm diameter and 40 cm height. Using equations 1.42 and 1.44 the diffusion coefficients characterizing the experiment can be evaluated. The provided values however should be considered a coarse approximation as the effect of a strong external magnetic field, typical of an HiPIMS experiment, has not yet been implemented in the Yacora Ar^+ model.

$$\begin{cases} \widetilde{\Lambda} = 0.3\,\mathrm{m} \\ \Lambda = 0.06\,\mathrm{m} \end{cases} \tag{4.5}$$

Figure 4.13 shows the ratio of the lines at 480.6 nm and 488.0 nm predicted by Yacora for a wide range of electron densities and the two extreme values of electron temperature. In this case the 2 eV curve provides a lower limit of the predicted range while the curve at 5 eV the upper one. Table 4.3 summarizes the predicted electron density corresponding to the two temperature extremes for the HiPIMS measurements listed in table 4.2.

The measured electron density is two orders of magnitude lower than the expected maximum value of $6 \times 10^{19}\,\mathrm{m}^{-3}$ near the sputtering target.

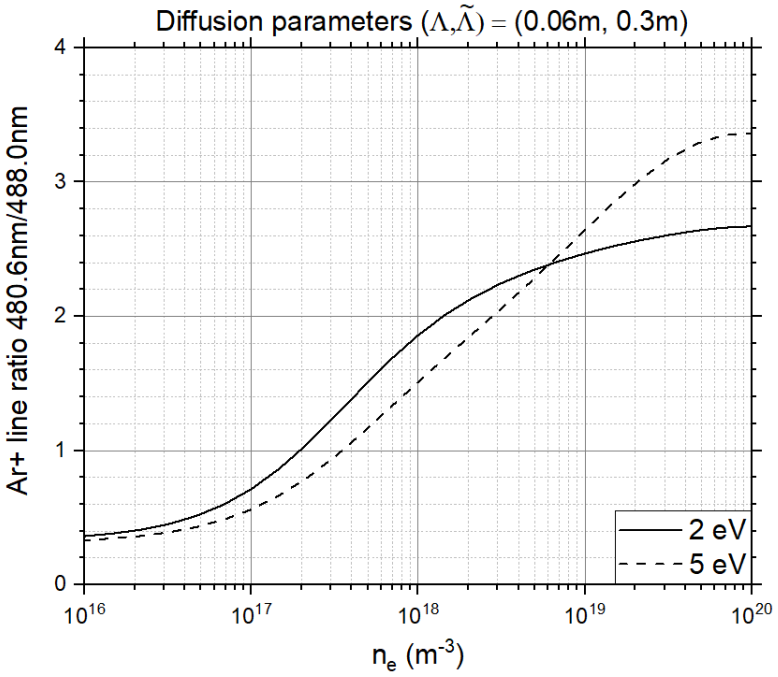

Figure 4.13: 480.6 nm and 488.0 nm line ratios at 2 eV and 5 eV predicted by Yacora. A pressure of 0.5 Pa and diffusion coefficients $\widetilde{\Lambda} = 0.3\,\mathrm{m}$, $\Lambda = 0.06\,\mathrm{m}$ are imposed.

Table 4.3: Electron density range for HiPIMS experiment predicted by Yacora.

Discharge Current (A)	n_e at 2 eV (m^{-3})	n_e at 5 eV (m^{-3})
10	1.6×10^{17}	2.9×10^{17}
20	3.5×10^{17}	6.6×10^{17}
30	3.5×10^{17}	6.6×10^{17}
40	4.3×10^{17}	8.3×10^{17}
54	3.5×10^{17}	6.6×10^{17}

A possible reason for such difference is the line of sight of the spectrometer. For the analysed spectra, the Echelle spectrometer position was parallel to the target. As mentioned in section 1.6.1, such plasma presents strong gradients of electron density Therefore the photons emitted by the region of the high density plasma trapped by magnetic field were observed together with lower electron densities regions. Thus, the OES analysis was performed on a non-homogeneous plasma and the ratio of the lines at 480.6 nm and 488.0 nm, and consequently the predicted electron density range, should be interpreted as an

average. In particular, the very weak variation of the line ratio measured for different peak discharge currents, which as already mentioned should increase the electron density of the magnetically confined plasma region, suggests a low sensibility of the line of sight average measurement on the electron density of such region. This, together with the diffusion parameters not taking into account the effects of magnetic fields, might explain why the Yacora Ar^+ model predicted an electron density two orders of magnitude lower than the reference value.

Chapter 5

Conclusions

The goals of this thesis were the creation and development of an Ar^+ collisional radiative (CR) model, for the optical emission spectroscopy (OES) measurements interpretation for plasmas containing argon, based on the flexible solver Yacora and its benchmark based both on a pre-existing CR model and on OES measurements of Ar plasmas.

In order to achieve this, the package Yacora was preferred to more widely used alternatives due to its flexibility in handling non linear, user defined, terms in the set of coupled equations.

The chosen input database was provided by a 2007 article by D. C. Griffin[30]. Since the energies of the 40 lowest excited Ar^+ states were the closest to the values provided on NIST database[4] such article was assumed to be the most accurate.

As starting point, a first version of the Yacora Ar^+ CR model, was created with the purpose of replicating the results, based on the same input database, of ADAS, a set of codes and data collection for modelling the radiation properties of emitting particles in plasmas.

Such first version, which included spontaneous emission and electron collision excitation and de-excitation succeeded in reproducing the predictions of ADAS model based on the same database. As it is discussed in the dedicated section, the two codes provide the same population coefficients in the corona equilibrium, which is typical for low electron densities. As for the local thermodynamic equilibrium region it is shown that some differences between the two codes might arise. The reasons for this is not entirely clear, but a possible explanation is the fact that ADAS, in order to simplify the set of differential equations, can bundle several excited high energy states to one state. This can influence lower energy states which are populated by spontaneous emissions from the bundled states. Such effect would be more noticeable for high electron densities and temperatures as the higher excited states become more populated.

The model was then improved by implementing an approximation for taking into account particle diffusion as a mean particle loss probability and elec-

tron collision ionization from states $1 - 3s^2 3p^5(^2P)$ (the ground state), $3 - 3s^2 3p^4(^3P)3d(^4D)$ and $6 - 3s^2 3p^4(^3P)3d(^4F)$. Both processes are needed since the metastable state, especially at lower electron densities where the effect of electron collision de-excitation is negligible, is highly influenced by diffusion, which is its main loss term in the coupled set of differential equation. This can indirectly influence also states sensitive to the metastable population coefficient, as it is shown for state $15 - 3p^4(^3P)4p(^2D)$, which is crucial since it is the upper state of the transition with wavelength 488.0 nm, which is widely used together with the line at 480.6 nm for the measurement by OES of line of sight averaged plasma parameters. On the other hand, electron collision ionization becomes crucial as the electron temperature increases since, as it is shown in an example, the rate coefficient for the ionization of Ar^+ ground state at about 20 eV becomes an order of magnitude higher that the most probable electron collision excitation rate coefficient.

Yacora Ar^+ model predictions were then compared with OES measurements for benchmarking in the electron density region between $1 \times 10^{17}\,m^{-3}$ and $1 \times 10^{18}\,m^{-3}$ and for electron temperatures between 2 eV and 7 eV done at the PlanICE experiment at EPP in the Department of Physics of University of Augsburg. Thanks to the information on electron temperature and density provided with a movable Langmuir probe, this benchmark of the model could be performed.

The assumptions on fine structure splitting and diffusion made in the model proved to be compatible with the OES measurements and the Yacora Ar^+ model successfully provided values compatible with the Langmuir porbe measurements. However, differences in the shape of the predicted electron densities and temperatures highlight that some processes might be missing in the Yacora Ar^+ model. Examples of the missing processes are heavy particles collisions, such as energy pooling and penning ionization, which are briefly discussed in the thesis, as well as electron collision ionization from additional Ar^+ states.

As for the HiPIMS experiment at the Institute for Electrical Engineering and Plasma Technology of Ruhr-University in Bochum, Yacora Ar^+ model was used to evaluate electron emission coefficients with little information on electron temperature and with an electron density of about $6 \times 10^{19}\,m^{-3}$ expected to be measured in the plasma trapped by the magnetron. Such benchmark was not successful as Yacora Ar^+ model predicts electron densities similar to those reached in PlanICE Ar plasmas.

An explanation for this is that OES measurements do not focus only on such region but, instead, provides information averaged over the line of sight of the spectrometer. This means that the prediction by the Yacora Ar^+ model based on OES are an average between the high electron density trapped plasma and lower electron density regions nearby, for which, no reference value was available. However, the benchmark with an HiPIMS experiment highlighted the importance of including the effects of a high magnetic field in the diffusion coefficients. This should be done as the very next step of the improvement of the Yacora Ar^+ model.

In conclusion, in order to complete the validation of the Yacora Ar^+ model, which proved to be reliable for the parameters covered by PlanICE, additional benchmarks of the Yacora model for Ar^+ at different plasma parameters, in particular at temperatures above 10 eV or at electron densities above $1 \times 10^{18}\,m^{-3}$, should be performed. For different plasma conditions the contribution of the mentioned additional processes can be required in the model and thus should be included.

Acknowledgements

I would like to thank my family as they greatly supported me during the entire Erasmus period. I would like to thank Prof. Ursel Fantz for all her precious suggestions to the work and for the opportunity of joining the IPP ITED group, where I've been warmly welcomed. A huge thanks goes to Dr. Dirk Wünderlich, my supervisor at IPP, as he was always willing to dedicate to me a lot of time for discussions about Yacora and the physics behind this thesis. I would also like to thank Dr. Gianluigi Serianni, who has always been available for advice both during the master and the bachelor thesis and proposed to me the opportunity of working on my master thesis during an Ereasmus period. A would like to thank also Dr. Thomas Pütterich, who greatly helped me in the understanding of ADAS. A special thanks goes to Caecilia Fröhler. She helped me with the acquisition of the spectra at PlanICE and provided the absolute calibration for them, making possible such an important benchmark to the Yacora Ar^+ collisional radiative model. I would really also like to thank Prof. Enrique Iglesias for providing me the spectra from the HiPIMS experiment together with detailed and very useful explanations on such experiment.

Bibliography

[1] U Fantz et al. "Spectroscopy—a powerful diagnostic tool in source development". In: *Nuclear Fusion* 46.6 (May 2006), S297–S306. DOI: 10.1088/0029-5515/46/6/s10. URL: https://doi.org/10.1088%2F0029-5515%2F46%2F6%2Fs10.

[2] B H Bransden and Charles Joachain. *Physics of Atoms and Molecules*. Ed. by Prentice Hall. Oct. 2014.

[3] Chemicool. *Aufbau Principle*. URL: https://www.chemicool.com/definition/aufbau-principle.html (visited on 2018).

[4] NIST. *Atomic Spectra Database*. URL: https://www.nist.gov/pml/atomic-spectra-database.

[5] N.H. List et al. "Beyond the electric-dipole approximation: A formulation and implementation of molecular response theory for the description of absorption of electromagnetic field radiation". In: *The Journal of Chemical Physics* 142.24 (2015), p. 244111. DOI: 10.1063/1.4922697.

[6] H. J. Wörner. *Lecture notes in Spectroscopy*. ETH Zurich.

[7] U Fantz. "Basics of plasma spectroscopy". In: *Plasma Sources Science and Technology* 15.4 (Oct. 2006), S137–S147. DOI: 10.1088/0963-0252/15/4/s01. URL: https://doi.org/10.1088%2F0963-0252%2F15%2F4%2Fs01.

[8] M. O'Brien. *Lecture notes in Astrophysical Processes*. UCL Astrophysics Group - London's Global University.

[9] D. Wünderlich, S. Dietrich, and U. Fantz. "Application of a collisional radiative model to atomic hydrogen for diagnostic purposes". In: *Journal of Quantitative Spectroscopy and Radiative Transfer* 110.1 (2009), pp. 62–71. ISSN: 0022-4073. DOI: https://doi.org/10.1016/j.jqsrt.2008.09.015. URL: http://www.sciencedirect.com/science/article/pii/S0022407308002082.

[10] ADAS. URL: http://www.adas.ac.uk/index.php.

[11] D. Saltzmann. *Atomic physics in hot plasmas*. Oxford University Press, 1998. ISBN: 0-19-510930-9.

[12] D C Griffin et al. "Electron-impact excitation and ionization of for the determination of impurity influx in tokamaks". In: *Journal of Physics B: Atomic, Molecular and Optical Physics* 30.15 (Aug. 1997), pp. 3543–3565. DOI: 10.1088/0953-4075/30/15/023. URL: https://doi.org/10.1088%2F0953-4075%2F30%2F15%2F023.

[13] T. Fujimoto. "Plasma Spectroscopy". In: *Plasma Polarization Spectroscopy*. Ed. by T. Fujimoto and A. Iwamae. Berlin, Heidelberg: Springer Berlin Heidelberg, 2008. ISBN: 978-3-540-73587-8. DOI: 10.1007/978-3-540-73587-8_3. URL: https://doi.org/10.1007/978-3-540-73587-8_3.

[14] W. Möller. "Plasma and surface modeling of the deposition of hydrogenated carbon films from low-pressure methane plasmas". In: *Applied Physics A* 56.6 (June 1993), pp. 527–546. ISSN: 1432-0630. DOI: 10.1007/BF00331402. URL: https://doi.org/10.1007/BF00331402.

[15] E J Iglesias et al. "In situ measurement of VUV/UV radiation from low-pressure microwave-produced plasma in Ar/O2gas mixtures". In: *Measurement Science and Technology* 28.8 (July 2017), p. 085501. DOI: 10.1088/1361-6501/aa7816. URL: https://doi.org/10.1088%2F1361-6501%2Faa7816.

[16] U. Fantz et al. "Quantification of the VUV radiation in low pressure hydrogen and nitrogen plasmas". In: *Plasma Sources Science and Technology* 25.4 (June 2016), p. 045006. DOI: 10.1088/0963-0252/25/4/045006. URL: https://doi.org/10.1088%2F0963-0252%2F25%2F4%2F045006.

[17] Inc. Materials Science. *Magnetron sputtering - TN 000 100 02/03*. Tech. rep.

[18] G Bräuer et al. "Magnetron Sputtering - Milestones of 30 Years". In: *Vacuum* 84 (June 2010), pp. 1354–1359. DOI: 10.1016/j.vacuum.2009.12.014.

[19] Inc. M. Hughes Semicore Equipment. *What is DC Sputtering?* URL: http://www.semicore.com/news/94-what-is-dc-sputtering.

[20] W. Kiyotaka, K. Isaku, and K. Hidetoshi. *Handbook of Sputtering Technology (Second Edition)*. Second Edition. Oxford: William Andrew Publishing, 2012. ISBN: 978-1-4377-3483-6. DOI: https://doi.org/10.1016/B978-1-4377-3483-6.00013-9. URL: http://www.sciencedirect.com/science/article/pii/B9781437734836000139.

[21] S. M. Meier et al. "First measurements of the temporal evolution of the plasma density in HiPIMS discharges using THz time domain spectroscopy". In: *Plasma Sources Science and Technology* 27.3 (Mar. 2018), p. 035006. DOI: 10.1088/1361-6595/aab188. URL: https://doi.org/10.1088%2F1361-6595%2Faab188.

[22] S. Briefi, P. Gutmann, and U. Fantz. "Alternative RF coupling configurations for H ion sources". In: *AIP Conference Proceedings* 1655.1 (2015), p. 040003. DOI: 10.1063/1.4916445. eprint: https://aip.scitation.org/doi/pdf/10.1063/1.4916445. URL: https://aip.scitation.org/doi/abs/10.1063/1.4916445.

[23] L. A. Whitehead and M. A. Mossman. "Jack O'Lanterns and integrating spheres: Halloween physics". In: *American Journal of Physics* 74.6 (2006), pp. 537–541. DOI: 10.1119/1.2190687. eprint: https://doi.org/10.1119/1.2190687. URL: https://doi.org/10.1119/1.2190687.

[24] J Held et al. "Velocity distribution of titanium neutrals in the target region of high power impulse magnetron sputtering discharges". In: *Plasma Sources Science and Technology* 27.10 (Oct. 2018), p. 105012. DOI: 10.1088/1361-6595/aae236. URL: https://doi.org/10.1088%2F1361-6595%2Faae236.

[25] *Private Communication by A. Hecimovic, Max-Planck-Institut für Plasmaphysik, Garching.*

[26] *Spectrum taken at HIPIMS experiment RUB-Experimental Physics II by Dr. E. Iglesias AEPT - RUB, with echelle spectrometer.*

[27] N Bibinov et al. "Relative and absolute intensity calibrations of a modern broadband echelle spectrometer". In: *Measurement Science and Technology* 18.5 (Mar. 2007), pp. 1327–1337. DOI: 10.1088/0957-0233/18/5/019. URL: https://doi.org/10.1088%2F0957-0233%2F18%2F5%2F019.

[28] D. Wünderlich, S. Dietrich, and U. Fantz. "Application of a collisional radiative model to atomic hydrogen for diagnostic purposes". In: *Journal of Quantitative Spectroscopy and Radiative Transfer* 110.1 (2009), pp. 62–71. ISSN: 0022-4073. DOI: https://doi.org/10.1016/j.jqsrt.2008.09.015. URL: http://www.sciencedirect.com/science/article/pii/S0022407308002082.

[29] S. D. Cohen and A. C. Hindmarsh. "CVODE, a Stiff/Nonstiff ODE Solver in C". In: *Comput. Phys.* 10.2 (Mar. 1996), pp. 138–143. ISSN: 0894-1866. DOI: 10.1063/1.4822377. URL: http://dx.doi.org/10.1063/1.4822377.

[30] D C Griffin et al. "Electron-impact excitation of Ar: an improved determination of Ar impurity influx in tokamaks". In: *Journal of Physics B: Atomic, Molecular and Optical Physics* 40.23 (Nov. 2007), pp. 4537–4550. DOI: 10.1088/0953-4075/40/23/013. URL: https://doi.org/10.1088%2F0953-4075%2F40%2F23%2F013.

[31] Open-ADAS. *Atomic Data and Analysis Structure Database.* URL: http://open.adas.ac.uk/.

[32] R.K. Janev et al. *Elementary Processes in Hydrogen-Helium Plasmas - Cross-sections and Reaction Rate Coefficients.* Vol. 4. Jan. 1987. DOI: 10.1007/978-3-642-71935-6.

[33] T. Fujimoto. "A collisional-radiative model for helium and its application to a discharge plasma". In: *Journal of Quantitative Spectroscopy and Radiative Transfer* 21.5 (1979), pp. 439–455. ISSN: 0022-4073. DOI: https://doi.org/10.1016/0022-4073(79)90004-9. URL: http://www.sciencedirect.com/science/article/pii/0022407379900049.

[34] A. Müller. "Ion Formation Processes: Ionization in Ion-Electron Collisions". In: Jan. 1991, pp. 13–90. DOI: 10.1007/978-3-642-84350-1_2.

[35] H.W. Ellis et al. "Transport properties of gaseous ions over a wide energy range". In: *Atomic Data and Nuclear Data Tables* 17.3 (1976), pp. 177–210. ISSN: 0092-640X. DOI: https://doi.org/10.1016/0092-640X(76)90001-2. URL: http://www.sciencedirect.com/science/article/pii/0092640X76900012.

[36] R. Berry. "The Theory of Penning Ionization". In: *Radiation research* 59 (Sept. 1974), pp. 367–75. DOI: 10.2307/3573984.

[37] P. Bicchi. "Energy-pooling reactions". In: *La Rivista del Nuovo Cimento (1978-1999)* 20.7 (July 1997), pp. 1–74. ISSN: 1826-9850. DOI: 10.1007/BF02879250. URL: https://doi.org/10.1007/BF02879250.

[38] *Private Communication by C. Fröhler, AG Experimentelle Plasmaphysik, Department of Physics, University of Augsburg.*

[39] A. Hecimovic et al. "Probing the electron density in HiPIMS plasmas by target inserts". In: *Journal of Physics D: Applied Physics* 50.50 (Nov. 2017), p. 505204. DOI: 10.1088/1361-6463/aa9914. URL: https://doi.org/10.1088%2F1361-6463%2Faa9914.